Origin and diversification of fibroblasts from the sclerotome in zebrafish

Roger C. Ma[1], Katrinka M. Kocha[1], Emilio E. Méndez-Olivos[1], Tyler D. Ruel[1], and Peng Huang[1]*

[1] Department of Biochemistry and Molecular Biology, Cumming School of Medicine, Alberta Children's Hospital Research Institute, University of Calgary, 3330 Hospital Drive, Calgary, Alberta, Canada T2N 4N1

* Correspondence should be addressed to PH.

Email: huangp@ucalgary.ca
Tel: 403-220-4612

Running title: Origin and diversification of fibroblasts

Keywords: Sclerotome, Fibroblasts, Collagen, Axial skeleton, Fin mesenchymal cells, Zebrafish

ABSTRACT

Fibroblasts play an important role in maintaining tissue integrity by secreting components of the extracellular matrix and initiating response to injury. Although the function of fibroblasts has been extensively studied in adults, the embryonic origin and diversification of different fibroblast subtypes during development remain largely unexplored. Using zebrafish as a model, we show that the sclerotome, a sub-compartment of the somite, is the embryonic source of multiple fibroblast subtypes including tenocytes (tendon fibroblasts), blood vessel associated fibroblasts, fin mesenchymal cells, and interstitial fibroblasts. High-resolution imaging shows that different fibroblast subtypes occupy unique anatomical locations with distinct morphologies. Long-term Cre-mediated lineage tracing reveals that the sclerotome also contributes to cells closely associated with the axial skeleton. Ablation of sclerotome progenitors results in extensive skeletal defects. Using photoconversion-based cell lineage analysis, we find that sclerotome progenitors at different dorsal-ventral and anterior-posterior positions display distinct differentiation potentials. Single-cell clonal analysis combined with in vivo imaging suggests that the sclerotome mostly contains unipotent and bipotent progenitors prior to cell migration, and the fate of their daughter cells is biased by their migration paths and relative positions. Together, our work demonstrates that the sclerotome is the embryonic source of trunk fibroblasts as well as the axial skeleton, and local signals likely contribute to the diversification of distinct fibroblast subtypes.

INTRODUCTION

Fibroblasts are connective tissue cells present in most organs of animals. They function as tissue support cells by synthesizing and remodeling the extracellular matrix (ECM). Recent studies have shown that tissue-resident fibroblasts also play important regulatory roles in wound healing, inflammation, tumor microenvironment, and tissue fibrosis (Kalluri, 2016; Kendall and Feghali-Bostwick, 2014; Plikus et al., 2021). Although fibroblasts have historically been viewed as a homogenous cell population, recent work using single-cell RNA sequencing (scRNA-seq) has revealed a high level of heterogeneity in fibroblast populations from different tissues as well as within the same tissue (Buechler et al., 2021; Forte et al., 2022; Muhl et al., 2020; Tabib et al., 2018; Xie et al., 2018). This raises the question of how the different fibroblast subtypes are generated during embryonic development.

One mechanism to diversify fibroblast populations is through contributions from multiple embryonic sources. Previous studies suggest that fibroblasts in the same tissue may have heterogeneous embryonic origins. For example, in avian and mouse embryos, dermal fibroblasts in the head are of neural crest origin, whereas those in the dorsal and ventral trunk originate from the somite and lateral plate mesoderm, respectively (Thulabandu et al., 2018). Similarly, during heart development in chick and mouse embryos, most cardiac fibroblasts originate from lateral plate mesoderm derived epicardium, while a small population arises from an endothelial/endocardial lineage (Tallquist, 2020).

Somites are the embryonic source of many tissue support cells, including fibroblasts (Christ et al., 2007). During development, somite forms three separate compartments: the dermatome, myotome, and sclerotome. The sclerotome contributes to the axial skeleton of animals (Christ et al., 2004). Work in mouse and chick has shown that the sclerotome is also the developmental origin of tendon fibroblasts (tenocytes) (Brent et al., 2003; Schweitzer et al., 2001) and vascular smooth muscle cells (Pouget et al., 2008; Wiegreffe et al., 2007). In zebrafish, the sclerotome has a unique bipartite organization and contributes to tenocytes, perivascular fibroblasts, and pericytes in a stereotypical manner (Ma et al., 2018; Rajan et al., 2020). It raises the question of the cellular mechanisms governing the diversification of fibroblast subtypes from sclerotome progenitors.

In fish and amphibians, fin mesenchymal cells are a population of fibroblasts present in the larval fin fold. They express many ECM proteins to provide structural support for the developing fin fold (Durán et al., 2011; Feitosa et al., 2012). However, the developmental origin of fin mesenchymal cells remains controversial. Dye labeling experiments in *Xenopus* and zebrafish suggest that the neural crest contributes to the fin mesenchyme (Smith and Hall, 1990; Smith et al., 1994). However, later

experiments in *Xenopus* suggest that the mesoderm also contributes to fin mesenchymal cells in both the dorsal and ventral fins (Garriock and Krieg, 2007; Tucker and Slack, 2004). Similarly, cell transplantation experiments in axolotls reveal dual origin of the fin mesenchyme from both the neural crest and somites (Sobkow et al., 2006). More recent work using genetic lineage tracing in fish (zebrafish) and amphibians (*Xenopus* and axolotl) supports a model where fin mesenchymal cells originate exclusively from the mesoderm with no contribution from the neural crest lineage (Lee et al., 2013; Taniguchi et al., 2015). In particular, the dermomyotome compartment of the somite has been suggested as the source of fin mesenchymal cells in zebrafish (Lee et al., 2013).

Here, we show that the sclerotome in zebrafish is a major source of multiple fibroblast populations as well as cells associated with the axial skeleton. Different sclerotome-derived fibroblast subtypes display unique morphologies and occupy distinct anatomical locations. In vivo time-lapse imaging and single-cell clonal analysis reveal that sclerotome progenitors can generate multiple fibroblast subtypes, and their differentiation potential is biased by their positions as well as their migratory patterns. Together, our results suggest that distinct fibroblast subtypes are specified from sclerotome progenitors by local cellular environments.

RESULTS

Characterization of a sclerotome reporter in zebrafish

To explore the lineage potential of the sclerotome in zebrafish, we recently developed a sclerotome reporter, *nkx3.1:Gal4; UAS:NTR-mCherry* (*nkx3.1*$^{NTR\text{-}mCherry}$) (Ma et al., 2018). The *nkx3.1:Gal4* driver accurately recapitulated the expression of the endogenous *nkx3.1* gene (Fig S1). The specificity of this *nkx3.1*$^{NTR\text{-}mCherry}$ line was further validated by co-labeling with known sclerotome markers, including *vcanb* (*versican b*) (Landolt et al., 1995), *foxc1b* (Topczewska et al., 2001), and *twist1b* (previously known as *twist1a*) (Germanguz et al., 2007; Yeo et al., 2009) (Fig 1A). Due to the perdurance of the mCherry protein, we used *nkx3.1*$^{NTR\text{-}mCherry}$ to label the initial sclerotome domains and all their descendants. We crossed *nkx3.1*$^{NTR\text{-}mCherry}$ with the endothelial reporter *kdrl:EGFP* to examine sclerotome-derived cells at 2 dpf (days post-fertilization). Based on the anatomical location and morphology, we broadly defined five groups of mCherry^{+} cells from the *nkx3.1* lineage (Fig 1B-C): 1) cells closely associated with blood vessels in the trunk, including the dorsal longitudinal anastomotic vessel (DLAV), intersegmental vessels (ISV), dorsal aorta (DA), and caudal vein plexus (CVP); 2) tenocytes along somite boundaries as previously described (Ma et al., 2018; Subramanian et al., 2018); 3) interstitial cells located in the space between the notochord, spinal cord, and muscles; 4) cells located in both dorsal and ventral fin folds; and 5) some muscle cells located at the dorsal and ventral edges of each somite (Ma et al., 2018). The contribution of muscles from the *nkx3.1* lineage suggests that *nkx3.1* labels some early bipotent somitic cells that generate both sclerotome progenitors and muscles, which is consistent with previous single-cell lineage analysis of the ventral somite (Morin-Kensicki and Eisen, 1997). In addition to the five groups of cells from the *nkx3.1* lineage, the *nkx3.1:Gal4* line drove ectopic expression in some cuboidal cells at the edge of the fin fold (Fig 1C and S2), which were not derived from the sclerotome. It is worth noting that although the *nkx3.1:Gal4* line nicely matched the endogenous *nkx3.1* expression, the amplification of the GAL4/UAS system in *nkx3.1*^{Kaede} (*nkx3.1:Gal4; UAS:Kaede*) and *nkx3.1*$^{NTR\text{-}mCherry}$ lines resulted in various degrees of ectopic expression outside the *nkx3.1* domains (Fig S1). We have previously shown that both tenocytes and ISV-associated perivascular fibroblasts express *col1a2* and *col5a1* (Ma et al., 2018; Rajan et al., 2020), two pan-fibroblast markers defined by scRNA-seq experiments (Metikala et al., 2021; Muhl et al., 2020). Indeed, all *nkx3.1*$^{NTR\text{-}mCherry}$-positive non-muscle cells (groups 1-4) were labeled by *col1a2:GFP* at 2 dpf (Fig 1D), confirming their fibroblast identity. Our results suggest that the sclerotome is the embryonic source of multiple types of fibroblasts in zebrafish.

The sclerotome generates different types of trunk fibroblasts

124 We performed mosaic labeling and marker analysis to characterize fibroblasts derived from the
125 *nkx3.1* lineage (Fig 2A-C). *nkx3.1*$^{NTR\text{-}mCherry}$-expressing fibroblasts in the trunk, including tenocytes,
126 blood vessel associated fibroblasts, and interstitial fibroblasts, were marked by pan-fibroblast markers
127 such as *tgfbi* and *col5a1* (Metikala et al., 2021; Muhl et al., 2020) (Fig 2B). A subset of these
128 sclerotome-derived fibroblasts was associated with different vascular beds (Fig 1C and 2A). We
129 previously described ISV-associated perivascular fibroblasts, characterized by a globular cell body
130 with short processes extending around the ISV (Rajan et al., 2020). By contrast, labeling with a
131 mosaic *col1a2:Gal4; UAS:Kaede* line (*col1a2*^{Kaede}) (Sharma et al., 2019) revealed that fibroblasts
132 associated with DLAV or DA (DLAV and DA fibroblasts, respectively) were more elongated along the
133 long axis of the blood vessel (Fig 1C and 2A). CVP is a transient venous network with a stereotypical
134 "honeycomb-like" structure. Fibroblasts marked by *nkx3.1*$^{NTR\text{-}mCherry}$ occupied the space in the
135 honeycomb pockets of the CVP (Fig 1C and 2A). Mosaic labeling showed that individual Kaede^{+} cells
136 had a small and elongated cell body with long cellular processes along the underlying endothelium
137 and sometimes across the honeycomb pocket (Fig 2A). The location and morphology of these CVP-
138 associated fibroblasts suggest that they are stromal reticular cells (SRCs) (Murayama et al., 2015).
139 Tenocytes and interstitial fibroblasts were the two fibroblast subtypes that populated the trunk
140 region but were not closely associated with blood vessels (Fig 1C). We and others have previously
141 shown that tenocytes are located along the myotendinous junction (MTJ), extending long cellular
142 processes into the intersomitic space (Fig 2A) (Ma et al., 2018; Subramanian et al., 2018). Marker
143 analysis revealed that *nkx3.1*$^{NTR\text{-}mCherry}$-positive cells along the MTJ were specifically labeled by known
144 tendon markers such as *scxa*, *cilp*, and *tnmd* (Chen and Galloway, 2014; Ralliere et al., 2015) (Fig
145 2C). By contrast, interstitial fibroblasts were scattered throughout the interstitial space and displayed
146 varied morphologies (Fig 1C and 2A).
147
148 **The sclerotome contributes to fin mesenchymal cells**
149 The *nkx3.1*$^{NTR\text{-}mCherry}$ line labeled cells in the fin fold (Fig 1B-C). At 2 dpf, the fin fold is subdivided
150 into two parts: the major lobe wrapping around the trunk and tail, and the minor lobe beneath the yolk
151 extension (Parichy et al., 2009) (Fig S2). Cells from the *nkx3.1* lineage populated both the dorsal and
152 ventral regions in the major lobe (Fig 1C and S2). Using the mosaic *col1a2*^{Kaede} line, we found that
153 Kaede^{+} fin cells displayed extensive "tree-like" cellular processes projecting towards the periphery of
154 the fin fold (Fig 2A). The location and morphology suggest that these sclerotome-derived fin fold
155 residing cells correspond to fin mesenchymal cells (Carney et al., 2010; Feitosa et al., 2012; Lee et
156 al., 2013). Previous studies have shown that fin mesenchymal cells are marked by *hemicentin2*
157 (*hmcn2*) and *fibulin1* (*fbln1*), while the neighboring cell layer of apical epidermal cells is labelled by

158 *hmcn2* and *fras1* (Carney et al., 2010; Feitosa et al., 2012; Lee et al., 2013) (Fig 3A). Double staining
159 revealed two juxtaposing cell layers in the fin fold: *hmcn2*$^{+}$*fbln1*$^{+}$ fin mesenchymal cells in the proximal
160 layer, and *hmcn2*$^{+}$*fras1*$^{+}$ apical epidermal cells in the distal layer (Fig 3B). As expected, double
161 staining in *nkx3.1*$^{NTR\text{-}mCherry}$ embryos showed that mCherry^{+} cells in the fin fold co-expressed *fbln1* but
162 not *fras1* (Fig 3C), confirming that the sclerotome contributes to fin mesenchymal cells, a specific cell
163 population in the fin fold.
164 Interestingly, *nkx3.1*^{Kaede}-expressing fin mesenchymal cells were absent in the caudal fin fold and
165 minor lobe (Fig S2). Cre-mediated lineage tracing in *nkx3.1:Gal4; UAS:Cre-ERT2; ubi:Switch* fish
166 showed similar results (Fig 3D). Switched mCherry^{+} cells derived from the *nkx3.1* lineage gave rise to
167 fin mesenchymal cells in both the dorsal and ventral regions of the major lobe at 4 dpf, but cells in the
168 minor lobe and caudal fin remained GFP^{+}mCherry^{-} (un-switched) (Fig 3D). Our results suggest that
169 sclerotome is not the only lineage that gives rise to fin mesenchymal cells. To determine whether the
170 dermomyotome (also known as the external cell layer) contributes to fin mesenchymal cells, we
171 imaged *pax7b:Gal4FF; UAS:EGFP* (*pax7b*^{EGFP}) fish at 50 hpf. Interestingly, despite extensive labeling
172 of dermomyotome cells in all somites, most fin mesenchymal cells were not marked by *pax7b*^{EGFP} (Fig
173 3E). EGFP^{+} fin cells were not observed in the minor lobe or caudal fin, while on average, only 4.6%
174 and 0.2% of fin mesenchymal cells were *pax7b*^{EGFP}-positive in the dorsal and ventral regions of the
175 major lobe, respectively (Fig 3F). This is in striking contrast to 95% (dorsal) and 94% (ventral)
176 contributions from the *nkx3.1*$^{NTR\text{-}mCherry}$ reporter (Fig 3F). Therefore, our results suggest that the
177 sclerotome, but not the dermomyotome, is the main contributor of fin mesenchymal cells in the dorsal
178 and ventral fin folds.
179 Together, our data show that the sclerotome generates multiple types of fibroblasts in the
180 zebrafish trunk, supporting different tissues such as muscles, blood vessels, and the fin fold. These
181 fibroblast subtypes reside in distinct anatomical locations with unique morphologies, some of which
182 can be defined by specific marker expression.
183
184 **The sclerotome contributes to the axial skeleton in zebrafish**
185 Since the sclerotome is known to contribute to the axial skeleton (Christ et al., 2004), we
186 performed Cre-mediated lineage tracing on cells from the *nkx3.1* lineage in zebrafish. Sclerotome-
187 derived cells in *nkx3.1:Gal4; UAS:Cre-ERT2; ubi:Switch* fish were switched to express mCherry with
188 4-hydroxytamoxifen (4OHT) treatment at 1-2 dpf. Co-labeling of calcein, a vital dye for calcified
189 structures, in switched fish at 17 dpf revealed that mCherry^{+} cells were closely associated with the
190 vertebrae, including the centrum, neural arch, and hemal arch (Fig 4A). Interestingly, mCherry^{+} cells
191 formed a thin layer external to the calcein-positive centrum, with enrichment in the region between

192 adjacent centra (Fig 4A). By contrast, calcein staining in neural and hemal arches appeared to be
193 embedded within mCherry^{+} cells with overlapping staining (Fig 4A). Long-term tracing of *nkx3.1*$^{+}$ cells
194 resulted in substantial labeling of tenocytes at the MTJ and cells associated with the vertebral column
195 in fish at 6 weeks post-fertilization (wpf) and adult stages (Fig 4B). To determine the function of
196 sclerotome-derived cells in skeletal development, we performed genetic ablation using the
197 nitroreductase (NTR) system (Curado et al., 2008). *nkx3.1*$^{NTR\text{-}mCherry}$ embryos or their mCherry^{-} siblings
198 were treated with metronidazole (MTZ) at 1-2 dpf and stained for bone and cartilage at 3 wpf (Fig 4C-
199 E). Since many ablated fish developed heart edema, likely caused by the depletion of perivascular
200 fibroblasts (Rajan et al., 2020), we can only analyze survivors from the ablated group, which likely
201 represents fish with more mosaic expression. MTZ-treated mCherry^{+} fish were significantly smaller
202 than mCherry^{-} controls (Fig 4D), suggesting impaired growth with partial ablation of the *nkx3.1*
203 lineage. Interestingly, while vertebral bodies formed normally, both neural and hemal arches displayed
204 variable defects, with an average of 35% of vertebrae missing neural arches and 3% missing hemal
205 arches (Fig 4C-E). Together, our results suggest that sclerotome-derived cells in zebrafish contribute
206 to the normal development of the vertebral column, especially skeletal elements attached to the
207 vertebral body.
208
209 **Both dorsal and ventral sclerotome domains give rise to multiple types of fibroblasts**
210 We have previously shown that the zebrafish sclerotome consists of a dorsal and ventral domain,
211 both of which generate tenocytes and perivascular fibroblasts (Ma et al., 2018; Rajan et al., 2020). We
212 asked how each sclerotome domain contributes to different fibroblast subtypes. Taking advantage of
213 the photoconvertible Kaede protein, we performed lineage tracing of sclerotome domains in
214 *nkx3.1*^{Kaede} fish (Fig 5A). Either the dorsal or ventral sclerotome domain of a single somite was
215 photoconverted from Kaede^{green} to Kaede^{red} at 24 hpf (hours post-fertilization). We then determined
216 the fate of Kaede^{red} cells after 24 hours based on their location and morphology.
217 When the dorsal sclerotome was labeled at 24 hpf, we observed small projections from these
218 Kaede^{red} cells, suggesting the initiation of cell migration at this stage (Fig 5B). At 48 hpf, all dorsal
219 sclerotome-derived Kaede^{red} cells were restricted to the upper half of the trunk dorsal to the notochord
220 (Fig 5B). Based on the morphology and location relative to the vasculature, we determined that the
221 dorsal sclerotome generated dorsal fin mesenchymal cells, DLAV fibroblasts, tenocytes, ISV-
222 associated perivascular fibroblasts, and interstitial fibroblasts.
223 Next, we performed photoconversion experiments to mark the ventral sclerotome with Kaede^{red} at
224 24 hpf. Similar to the dorsal domain, small cellular projections were visible from Kaede^{red} cells,
225 suggesting that both dorsal and ventral sclerotome progenitors initiate their migration at the same

226 stage (Fig 5C). Interestingly, in anteriorly converted somites (somites 16-18), cellular projections
227 pointed exclusively in the dorsal direction, while in posteriorly converted somites (somites 23-25), both
228 dorsal and ventral projections were observed (Fig 5C). This result suggests that the migration pattern
229 is different in ventral sclerotome progenitors along the anterior-posterior axis, which likely accounts for
230 the cells generated in the CVP and ventral fin fold region. All the cells generated by the ventral
231 sclerotome were restricted to approximately the ventral two-thirds of the trunk. In anterior somites, the
232 ventral sclerotome generated cells in the trunk, including tenocytes, perivascular fibroblasts, and
233 interstitial fibroblasts at 48 hpf (Fig 5C). In contrast, the ventral sclerotome of posterior somites gave
234 rise to cells in the trunk and cells ventral to the photoconverted region in the periphery, including CVP-
235 associated SRCs and fin mesenchymal cells in the ventral fin fold (Fig 5C).
236 Together, our results suggest that both the dorsal and ventral sclerotome domains can generate
237 multiple fibroblast subtypes, but the progenitors in each domain generate an anatomically restricted
238 population of cells according to their dorsal-ventral and anterior-posterior positions.
239
240 **Fate of dorsal sclerotome progenitors is biased by the migration direction**
241 Both dorsal and ventral sclerotome contribute to multiple types of fibroblasts. It is possible that
242 sclerotome progenitors are multipotent, or alternatively, individual progenitors are "fate-restricted" to
243 differentiate into a specific fibroblast subtype. To distinguish these possibilities, we performed single-
244 cell clonal analysis of sclerotome progenitors as previously described (Sharma et al., 2019). We
245 focused on the smaller dorsal domain to ensure precise single-cell photoconversion and accurate cell
246 tracing. We selected *nkx3.1*^{Kaede} fish with more mosaic Kaede expression to minimize the
247 photoconversion of multiple cells. At 24 hpf, a single Kaede^{green} cell in the dorsal domain between
248 somites 16 and 18 was photoconverted to Kaede^{red} (Fig 6A). We then imaged the same fish after 24
249 hours to determine the identity of their Kaede^{red} descendants. Most clones (35/42, 83%) contained at
250 least 2 daughter cells, suggesting at least one cell division between 24 and 48 hpf (Fig 6B). From 42
251 dorsal sclerotome progenitors, 38% (16/42) produced clones with at least two fibroblast subtypes, and
252 2% (1/42) generated three subtypes (Fig 6C). This result suggests that some dorsal sclerotome
253 progenitors are bipotent and possibly multipotent at 24 hpf. Consistent with domain tracing, we found
254 that dorsal sclerotome progenitors gave rise to all four types of fibroblasts, including dorsal fin
255 mesenchymal cells, tenocytes, blood vessel associated fibroblasts, and interstitial fibroblasts (Fig 6D).
256 As observed earlier, 33 of the 42 photoconverted Kaede^{red} cells at 24 hpf showed visibly biased
257 projections pointing either dorsally (14 cells) or ventrally (19 cells), likely corresponding to their
258 migration direction. To correlate progenitor morphology with their lineage potential, we categorized
259 different fibroblasts into two types based on their final positions (Fig 6A). In the type I group,

260 fibroblasts are located dorsal to the somite, including dorsal fin mesenchymal cells and DLAV
261 fibroblasts. Type II cells, such as tenocytes, ISV-associated perivascular fibroblasts, and interstitial
262 fibroblasts, are located medial to the somite. Interestingly, progenitors with initial dorsal projections
263 predominantly generated type I cells (13/14, 93%), whereas cells projecting ventrally were more likely
264 to give rise to type II cells (11/19, 58%) than type I cells (3/19, 16%) and sometimes generated cells of
265 both types (5/19, 26%) (Fig 6E-F). It is important to note that ventral projecting progenitors at 24 hpf
266 never generated dorsal fin mesenchymal cells and all type I cells generated by this group were DLAV
267 fibroblasts found along the ventral side of the DLAV (Fig 6F). Together, our results suggest that the
268 dorsal sclerotome domain contains a mixture of unipotent and bipotent progenitors at 24 hpf, and their
269 migration direction likely restricts the types of fibroblasts they differentiate into.
270
271 **Fate of ventral sclerotome progenitors is biased by the position along the migratory path**
272 In posterior somites, some ventral sclerotome progenitors migrate ventrally towards the CVP
273 region to generate SRCs and ventral fin mesenchymal cells. To visualize this dynamic process, we
274 performed time-lapse imaging of *kdrl:EGFP; nkx3.1*$^{NTR\text{-}mCherry}$ embryos from 25 to 50 hpf (Video S1
275 and Fig S3). At 25 hpf, some migrating mCherry^{+} progenitors were found ventral to the somites.
276 These cells migrated ventrally towards the fin fold as more mCherry^{+} cells emerged from the ventral
277 somite and joined the migration. To better describe the position of migrating cells, we referred to cells
278 at the front edge of the migration as “leading cells”, while all cells behind were called “lagging cells”.
279 We observed a stereotypical migration pattern whereby mCherry^{+} cells “marched” ventrally in an
280 orderly fashion, and individual cells did not pass other cells that were ahead. This orderly migration
281 was largely maintained, even during cell division. As a result, descendants of leading cells remained
282 at the front of the migration throughout the movie and formed ventral fin mesenchymal cells, whereas
283 descendants of lagging cells mostly generated SRCs associated with the CVP (Video S1 and Fig S3).
284 Interestingly, the cardinal vein underwent similar ventral expansion to form the CVP during the same
285 time window. Lagging cells appeared to constantly interact with the forming CVP, while leading cells
286 remained ahead of the vascular sprouts (Video S1 and Fig S3). Together, our results suggest that the
287 fate of ventral sclerotome progenitors is biased by their position along the migratory path, potentially
288 due to their interactions with the local environment.
289 To further compare the lineage potential between the leading and lagging cells, we performed
290 single-cell clonal analysis in *nkx3.1*^{Kaede} fish (Fig 7A). Single ventrally migrating Kaede^{green} progenitors
291 between somites 21-25 were photoconverted to Kaede^{red} at 24 hpf, and their descendants were
292 imaged after 24 hours. Similar to our time-lapse movies, the majority of photoconverted leading cells
293 generated only ventral fin mesenchymal cells (17/20, 85%), but a small number gave rise to both

294 SRCs and ventral fin mesenchymal cells (3/20, 15%) (Fig 7B-C). Interestingly, leading cells never
295 generated SRCs only. By contrast, 41% of lagging cells generated only SRCs (9/22), 36% generated
296 both ventral fin mesenchymal cells and SRCs (8/22), and 23% produced only ventral fin mesenchymal
297 cells (5/22) (Fig 7B-C). Combining time-lapse imaging and single-cell tracing, our results suggest that
298 the relative position along the migratory path biases the fate of these sclerotome-derived cells.

DISCUSSION

Our work establishes the sclerotome as the embryonic source of different connective tissue cells in zebrafish. First, the sclerotome gives rise to distinct fibroblasts in the trunk. Second, the sclerotome contributes to proper development of the axial skeleton. Third, the sclerotome contains a mixture of unipotent and bipotent progenitors and their differentiation is biased by their axial positions and migratory paths.

The sclerotome is the embryonic source of trunk fibroblasts

The developmental potential of the sclerotome in zebrafish has been first explored with vital dye injections (Morin-Kensicki and Eisen, 1997). Using a classic sclerotome marker *nkx3.1* (Schneider et al., 2000), we have previously developed the *nkx3.1:Gal4* line in zebrafish to genetically label sclerotome progenitors and their descendants (Ma et al., 2018). Here, we provide additional evidence that *nkx3.1:Gal4* labels cells of the sclerotome lineage. First, the *nkx3.1*$^{NTR\text{-}mCherry}$ reporter co-expresses known sclerotome markers such as *versican b* (Landolt et al., 1995), *foxc1b* (Topczewska et al., 2001), and *twist1b* (Germanguz et al., 2007; Yeo et al., 2009). Second, lineage tracing of *nkx3.1*-derived cells shows extensive labeling of cells associated with the axial skeleton, consistent with previous cell tracing experiments (Morin-Kensicki et al., 2002). Interestingly, the *nkx3.1*$^{NTR\text{-}mCherry}$ reporter also labels some muscles adjacent to the dorsal and ventral sclerotome domains. This observation is in agreement with previous single-cell lineage analysis of the presumptive sclerotome in the ventral somite where a sub-population of these cells gives rise to both sclerotome derivatives and muscles (Morin-Kensicki and Eisen, 1997). We speculate that some bipotent somitic cells might transiently express *nkx3.1*, before committing to either the myotome or the sclerotome lineage. This idea is supported by the observation that progenitors at developmental branch points sometimes express markers characteristic of multiple fates (Farrell et al., 2018).

Our previous studies (Ma et al., 2018; Rajan et al., 2020) and current work provide strong evidence that the sclerotome is the embryonic source of multiple types of fibroblasts in the trunk of zebrafish. Based on marker expression, anatomical location, cell morphology, and function, we define at least four fibroblast subtypes derived from the sclerotome: tenocytes, fin mesenchymal cells, blood vessel associated fibroblasts, and interstitial fibroblasts. Tenocytes express classic tendon markers *scxa* and *tnmd* (Chen and Galloway, 2014; Ma et al., 2018). Their cell bodies are positioned medially along the myotendinous junction, while extending long cellular processes into the intersomitic space (Ma et al., 2018; Subramanian et al., 2018). Tenocytes stabilize muscle attachment likely by secreting a number of ECM proteins (Ma et al., 2018; Subramanian and Schilling, 2014). Fin mesenchymal

333 cells, on the other hand, are marked by the expression of ECM genes *hmcn2* and *fbln1*. They are
334 located adjacent to apical epidermal cells in the fin fold with distally extended tree-like processes.
335 Recent work has shown that fin mesenchymal cells guide fin formation by aligning collagen fibers of
336 actinotrichia (Kuroda et al., 2020). Genetic ablation of fin mesenchymal cells in the pectoral and
337 median fin folds results in collapse of the respective fins (Lalonde and Akimenko, 2018). Although
338 blood vessel associated fibroblasts are labeled by pan-fibroblast markers similar as other fibroblast
339 subtypes in the trunk, they are characterized by their close association with the vasculature.
340 Interestingly, their morphology differs depending on the vascular bed. For example, ISV-associated
341 perivascular fibroblasts are globular, whereas DLAV fibroblasts are more elongated. We have
342 previously shown that perivascular fibroblasts play dual roles in stabilizing nascent ISVs and
343 functioning as pericyte precursors (Rajan et al., 2020). It is likely that other blood vessel associated
344 fibroblasts play similar roles in stabilizing the corresponding blood vessels. Interestingly, stromal
345 reticular cells closely interact with CVP, which functions as an early hematopoietic niche during
346 development (Wattrus and Zon, 2018). Indeed, recent work has shown that defects in SRC maturation
347 result in a compromised CVP niche that fails to support hematopoietic stem cell (HSC) maintenance
348 and expansion (Murayama et al., 2015). Therefore, SRCs might not only provide structural support to
349 the CVP, but also modulate the microenvironment required for HSC differentiation. Despite extensive
350 labeling of blood vessel associated fibroblasts, our lineage analysis shows that sclerotome
351 progenitors do not contribute to the vasculature. This result suggests that the sclerotome domain
352 defined by *nkx3.1* is distinct from the endotome, a sub-compartment of the somite that has been
353 shown to contain endothelial precursors (Nguyen et al., 2014; Sahai-Hernandez et al., 2020).
354 Compared to other fibroblast subtypes, interstitial fibroblasts are the least well-characterized. Based
355 on their distribution around the notochord and spinal cord, it is conceivable that interstitial fibroblasts
356 give rise to osteoblasts required for vertebral column development. This is consistent with our
357 observation that long-term cell tracing of the *nkx3.1* lineage results in extensive labeling of cells
358 associated with the vertebral bodies, neural and hemal arches. Together, our results suggest that the
359 sclerotome generates distinct fibroblast subtypes to support a variety of tissues, including muscles, fin
360 folds and blood vessels.
361
362 **The sclerotome contributes to axial skeleton development in zebrafish**
363 In amniotes, the sclerotome is the embryonic source of the vertebrae, structural units of the
364 vertebral column (Christ et al., 2004). In teleosts, each vertebra is composed of three elements:
365 vertebral body (centrum), neural, and hemal arches. In contrast to amniotes, studies in zebrafish and
366 salmon have suggested that the centrum is formed by notochord sheath cells instead of the

367 sclerotome (Fleming et al., 2004; Grotmol et al., 2003; Lleras Forero et al., 2018; Pogoda et al., 2018;
368 Wang et al., 2013; Wopat et al., 2018). However, how the sclerotome contributes to the development
369 of the axial skeleton in teleosts remains unclear. Our long-term lineage tracing experiments
370 demonstrate that cells derived from the sclerotome lineage are closely associated with all three
371 skeletal elements of the vertebrae. Partial depletion of sclerotome-derived cells results in variable
372 defects in neural and hemal arches, while centra are largely normal. This result is consistent with the
373 current model, in which the centrum forms independently of the somite (Lleras Forero et al., 2018;
374 Wopat et al., 2018). However, it is not clear why sclerotome ablation leads to a stronger defect in
375 neural arches than hemal arches, despite similar labeling of sclerotome-derived cells on both
376 structures. There are three non-mutually exclusive explanations. First, severe loss of hemal arches
377 might be detrimental to survival; therefore, only fish with mild phenotypes can survive to 3 wpf (time of
378 analysis). Second, the precursors of hemal arches might have a greater capacity to regenerate after
379 ablation than those of neural arches. Finally, there might be an alternative non-sclerotome source that
380 contributes to the formation of hemal arches redundantly. Interestingly, our results in zebrafish show
381 remarkable parallel to previous observations in medaka. In medaka, sclerotome-derived cells marked
382 by *twist:GFP* are similarly enriched in the intervertebral regions, and are thought to be the source of
383 osteoblasts to generate different skeletal elements (Inohaya et al., 2007). Morpholino knockdown of
384 key sclerotome genes, including *pax1*, *pax9*, and *twist*, results in the loss of neural arches with largely
385 normal centra (Mise et al., 2008; Yasutake et al., 2004). Together, these results suggest that the
386 sclerotome contributes to proper development of the axial skeleton in teleosts.
387
388 **The developmental origin of fin mesenchymal cells**
389 There has been considerable debate regarding where fin mesenchymal cells originate during fish
390 and amphibian development. Lineage tracing studies in zebrafish suggest that the paraxial
391 mesoderm, specifically the dermomyotome, but not the sclerotome, is the embryonic source of fin
392 mesenchymal cells (Lee et al., 2013). Their conclusions contrast with our findings in two aspects.
393 First, using the *pax3a:EGFP* line as a marker for the dermomyotome, Lee et al. (2013) show
394 extensive contribution of $EGFP^{+}$ fin mesenchymal cells throughout the entire major lobe of the fin fold,
395 including the caudal fin. By contrast, we find that a different dermomyotome reporter, $pax7b^{EGFP}$
396 (Pipalia et al., 2016), contributes minimally to fin mesenchymal cells in the fin fold. This discrepancy is
397 likely due to the different expression dynamics of *pax3a* and *pax7b*, despite both being
398 dermomyotome markers. It has been shown that *pax3a* is initially broadly expressed in the entire
399 somite before becoming restricted to the anterior somites (precursors of the dermomyotome) (Feng et
400 al., 2006; Hammond et al., 2007). However, *pax7b* is expressed several hours after *pax3a* and is

401 restricted to the anterior somites (Feng et al., 2006; Hammond et al., 2007; Minchin and Hughes,
402 2008). Therefore, the *pax3a:EGFP* line may not be as specific as *pax7b*^{EGFP} in labeling the
403 dermomyotome. Second, Lee et al. (2013) use the *ola-twist1:Gal4* transgenic line, in which Gal4
404 expression is driven by the medaka (*Oryzias latipes*) *twist1* promoter, to rule out sclerotome
405 contribution. However, our results using the *nkx3.1*$^{NTR\text{-}mCherry}$ reporter indicate that the sclerotome
406 contributes to most fin mesenchymal cells in both the dorsal and ventral regions of the major lobe.
407 Interestingly, we have previously shown that the expression of a similar *ola-twist1:EGFP* reporter is
408 restricted to sclerotome-derived cells around the notochord, but is absent in both dorsal and ventral
409 sclerotome domains (Ma et al., 2018). This observation explains why the *ola-twist1:Gal4* line fails to
410 label any fin mesenchymal cells (Lee et al., 2013). Together, our work suggests an updated model
411 where fin mesenchymal cells are generated by multiple lineages, depending on their locations. Fin
412 mesenchymal cells in the dorsal and ventral fin fold have a sclerotome origin, those in the caudal fin
413 originate from a non-dermomyotome and non-sclerotome compartment of the somite, while fin
414 mesenchymal cells in the minor lobe of the fin fold have an unidentified embryonic source.
415
416 **Mechanisms of fibroblast diversification**
417 A fundamental question in developmental biology is how progenitors in the embryo diversify into
418 distinct differentiated cell types. Using *nkx3.1*-based transgenic reporters, our work reveals three key
419 features of cell fate diversification from the sclerotome lineage (Fig 7D). First, sclerotome progenitors
420 display regional differences in their differentiation potential along the dorsal-ventral and anterior-
421 posterior positions. Dorsally located fibroblasts, such as dorsal fin mesenchymal cells and DLAV
422 fibroblasts, are derived from the dorsal sclerotome, whereas ventrally located fibroblasts, such as
423 stromal reticular cells and ventral fin mesenchymal cells, are generated by the ventral sclerotome.
424 Similarly, the ventral sclerotome in anterior somites (before the end of the yolk extension) generates
425 only fibroblasts in the trunk, whereas the ventral sclerotome in posterior somites contributes to stromal
426 reticular cells and fin mesenchymal cells in addition to trunk fibroblasts. Second, fate of sclerotome
427 progenitors is biased by their migratory path. For dorsal sclerotome progenitors, dorsal migration
428 limits the cell to become either dorsal fin mesenchymal cells or DLAV fibroblasts, while ventral
429 migration leads to the differentiation of predominately tenocytes or perivascular fibroblasts. Third, the
430 relative order of migrating sclerotome progenitors highly correlates with their differentiation potential.
431 Leading cells are more likely to become ventral fin mesenchymal cells, while lagging cells tend to
432 differentiate into stromal reticular cells. The combination of these three mechanisms (spatial
433 regulation, migration direction, and migration order) (Fig 7D) likely contributes to the generation of
434 different fibroblast subtypes in a stereotypical manner (Ma et al., 2018; Rajan et al., 2020).

How does a sclerotome progenitor decide which cell type to differentiate into? Photoconversion-based clonal analysis reveals that single sclerotome progenitors predominantly generate 1-2 different fibroblast subtypes. This result suggests that the sclerotome contains a mixture of unipotent and bipotent progenitors prior to migration. The presence of bipotent progenitors suggests that individual sclerotome cells are plastic and are not fate-restricted to become a specific fibroblast subtype. We speculate that the local microenvironment plays a key role in regulating the migration and subsequent differentiation of sclerotome-derived cells. In the trunk region, the migration of sclerotome-derived cells depends on Sonic Hedgehog (Shh) from the notochord and floor plate (Ma et al., 2018). Inhibition of Shh signaling results in the loss of tenocytes between muscle boundaries (Ma et al., 2018). Similarly, Slit-Robo signaling has been shown to mediate the polarization and migration of fin mesenchymal cells in the peripheral fin fold (Mahabaleshwar et al., 2022). Cell type diversification of the sclerotome is remarkably similar to that of the neural crest lineage. Previous studies have shown that migrating neural crest cells are multipotent (Baggiolini et al., 2015), and the ultimate cell fate is determined by their axial positions as well as the migration timing and direction (Rocha et al., 2020).

In summary, we demonstrate that the sclerotome is the embryonic source of multiple fibroblast subtypes and contributes to axial skeletal development in zebrafish. Our work shows that the sclerotome is an excellent model for studying cell type diversification during embryonic development. The combination of positional and migratory information as well as the local microenvironment likely contributes to the differentiation trajectory of sclerotome progenitors. Future work using scRNA-seq may further reveal the heterogeneity of sclerotome-derived cells and identify key gene regulatory networks underlying the lineage progression of sclerotome progenitors.

457 **MATERIALS AND METHODS**

458

459 **Ethics statement**

460 All animal experiments were conducted in accordance with the principles outlined in the current
461 Guidelines of the Canadian Council on Animal Care. All protocols were approved by the Animal Care
462 Committee of the University of Calgary (#AC17-0128 and #AC21-0102).

463

464 **Zebrafish strains**

465 Zebrafish strains used in this study were maintained and raised under standard conditions. The
466 following transgenic strains were used in this study: *Gt(:gSAIz-GAL4FFD)nkgsaizGFFD164A*
467 (*pax7b:Gal4FF*) (Pipalia et al., 2016), *TgBAC(col1a2:Gal4)ca102* (Ma et al., 2018; Sharma et al.,
468 2019), *TgBAC(col1a2:GFP)ca103* (Ma et al., 2018), *Tg(kdrl:EGFP)la163* (Choi et al., 2007),
469 *Tg(kdrl:mCherry)ci5* (Proulx et al., 2010), *TgBAC(nkx3.1:Gal4)ca101* (Ma et al., 2018),
470 *Tg(UAS:EGFP)nkuasgfp1a* (Asakawa et al., 2008), *Tg(UAS:Cre-ERT2)ca105* (Sharma et al., 2019),
471 *Tg(-3.5ubb:LOXP-EGFP-LOXP-mCherry)cz1701* (*ubi:Switch*) (Mosimann et al., 2011),
472 *Tg(UAS:Kaede)s1999t* (Davison et al., 2007), and *Tg(UAS:NTR-mCherry)c264* (Davison et al., 2007).
473 The mosaic *col1a2:Gal4; UAS:Kaede* line was maintained by selecting embryos with more mosaic
474 Kaede expression.

475

476 **In situ hybridization and immunohistochemistry**

477 Whole-mount in situ hybridization and immunohistochemistry were performed according to
478 previously established protocols. We used the following RNA probes in this study: *cilp*, *col5a1*, *fbln1*,
479 *foxc1b*, *fras1*, *gal4*, *hmcn2*, *kaede*, *ntr-mCherry*, *scxa*, *tgfbi*, *tnmd*, *twist1b, vcanb* (*versican b*). Double
480 fluorescent in situ hybridizations were performed using different combinations of digoxigenin (DIG) or
481 dinitrophenyl (DNP) labeled probes. For immunohistochemistry, rabbit polyclonal antibody to RFP
482 (1:1000, MBL, PM005) and chicken antibody to GFP (1:250, Aves Labs, GFP-1020) were used. For
483 fluorescent detection of antibody labeling, the appropriate Alexa Fluor-568 or Alexa Fluor-647
484 conjugated secondary antibodies (1:500, Thermo Fisher) were used.

485

486 **Kaede photoconversion**

487 Photoconversion was carried out using a 405 nm laser and a 20x objective on an Olympus
488 FV1200 confocal microscope. At the appropriate stage, Kaede-expressing embryos were
489 anesthetized using tricaine and mounted in 0.8% low-melting-point agarose. The duration and
490 intensity of laser required for complete green-to-red conversion depended on the Kaede expression

491 level and the size of the target region. For cell tracing of the sclerotome domains, a circular region of
492 20x20 pixels was converted using 1.5% 405 nm laser for 4 seconds. For single-cell clonal analysis of
493 sclerotome progenitors, typically a circular region of 10x10 pixels was converted using 1.5% 405 nm
494 laser for 4 seconds. After photoconversion, embryos were confirmed for the expression of Kaede^{red}
495 and recovered in E3 fish water until the necessary stages.
496
497 **Cre-mediated lineage tracing**
498 *nkx3.1:Gal4; UAS:Cre-ERT2; ubi:Switch* embryos were treated with 10 μM 4-hydroxytamoxifen
499 (4OHT) from 1 to 2 dpf. After treatment, embryos were washed three times and recovered in fish
500 water for analysis at the appropriate stages.
501
502 **Cell ablation**
503 NTR-mCherry^{+} embryos and NTR-mCherry^{-} sibling controls at the appropriate stage were treated
504 with metronidazole (MTZ, Sigma Millipore) at a concentration of 5 mM in fish water. Embryos were
505 incubated in MTZ solution for at least 24 hours to achieve complete ablation. Fish were then washed
506 and recovered in fish water until the desired stage for analysis.
507
508 **Bone and cartilage staining**
509 Bone and cartilage staining was performed following a modified version of a previously described
510 protocol (Walker and Kimmel, 2007). Briefly, larvae at 3 wpf were euthanized in 0.4% tricaine and
511 fixed in 4% formaldehyde in PBS overnight at 4 °C. Fixed larvae were washed in a solution containing
512 100 mM Tris pH 7.5 and 10 mM $MgCl_2$, then stained overnight in 0.04% alcian blue solution. The
513 larvae were then washed with decreasing concentrations of ethanol diluted in 100 mM Tris pH 7.5
514 (80%, 50%, 25%) and bleached in a 3% H_2O_2/0.5% KOH solution until all pigments were lost. They
515 were washed twice with 25% glycerol/0.1% KOH and stained in the same solution with 0.01% alizarin
516 red for 1 hour. Finally, larvae were washed twice in 50% glycerol/0.1% KOH and switched to 100%
517 glycerol for imaging.
518
519 **Calcein staining**
520 Bones can be fluorescently labelled in live larvae using the vital dye, calcein. Larvae at 17 dpf
521 were placed in a 100 mm petri dish in a 0.2% calcein solution for 15 – 30 minutes at room
522 temperature. They were then washed at least six times with water from zebrafish vivarium. The larvae
523 were left for 2 – 3 hours prior to imaging to allow excess calcein to pass through their digestive tract.

524 Fish were anesthetized using tricaine and mounted in 0.8% low-melting-point agarose for live
525 imaging. To obtain transverse views, fish were fixed in 4% formaldehyde and sectioned for imaging.
526
527 **Vibratome sectioning**
528 Juvenile and adult zebrafish were fixed in 4% paraformaldehyde (PFA) with 1% dimethyl sulfoxide
529 (DMSO) overnight at 4 °C. Fixed fish were washed in PBS and decalcified in 0.5 M EDTA at room
530 temperature for 3 days. Following decalcification, the dissected trunks were embedded in 20% gelatin
531 and sectioned using a Leica VT1000S vibratome to obtain slices at 150 µm thick. The sections were
532 mounted on slides in 50% glycerol for confocal imaging. Confocal tile scans were stitched together
533 using Olympus Fluoview software to generate a full view of the transverse section.
534
535 **Time-lapse imaging and cell tracking**
536 Time-lapse imaging of zebrafish embryos was carried out using an Olympus FV1200 confocal
537 microscope. At the appropriate stage, fish were anesthetized using tricaine and mounted in 0.8% low-
538 melting-point agarose. To keep the agarose hydrated and minimize the development of pigments, as
539 well as minimize movement of the fish, a small volume of E3 water with phenylthiourea and tricaine
540 was carefully flooded around the agarose. Z-stack images of the region of interest were collected at
541 regular intervals (6-9 mins) for up to 25 hours. Images were then compiled into movies using Olympus
542 Fluoview software. Cells from each movie were manually tracked using the Fiji software (Schindelin et
543 al., 2012).
544
545 **Statistical analysis**
546 All graphs were generated using the GraphPad Prism software. Data were plotted as mean±SEM.
547 The significance between two samples was calculated using Mann-Whitney *U* test. p values: $p>0.05$
548 (not significant); $p<0.05$ (*); $p<0.01$ (**); $p<0.001$ (***); $p<0.0001$ (****).

549 **ACKNOWLEDGMENTS**

550

551 We thank the zebrafish community for providing probes and reagents; Simon Hughes for sharing
552 the *pax7b*^{EGFP} line; Sarah Childs for sharing reagents, transgenic lines and providing critical input on
553 this project; members of the Childs and Huang laboratories for discussions; Arsheen Rajan for critical
554 comments on the manuscript.

555

556

557 **COMPETING INTERESTS**

558

559 The authors declare that no competing interests exist.

560

561

562 **FUNDING**

563

564 This study was supported by grants to P.H. from the Canadian Institute of Health Research (MOP-
565 136926 and PJT-169113), Canada Foundation for Innovation John R. Evans Leaders Fund (Project
566 32920), and Startup Fund from the Alberta Children's Hospital Research Institute (ACHRI).

567 **FIGURE LEGENDS**

568

569 **Fig 1. The sclerotome gives rise to different types of fibroblasts.** (A) Double fluorescent in situ
570 staining of *nkx3.1*$^{NTR\text{-}mCherry}$ embryos at 24 hpf showed co-expression of the sclerotome markers
571 *versican b*, *foxc1b*, and *twist1b* (cyan) with *ntr-mcherry* (red) in the dorsal sclerotome (short arrows),
572 ventral sclerotome (long arrows), and sclerotome-derived notochord-associated cells (arrowheads).
573 *n*=15 per staining. (B) Schematic of sclerotome-derived fibroblasts: blood vessel associated
574 fibroblasts (cyan), fin mesenchymal cells (black), tenocytes (magenta), and interstitial fibroblasts
575 (yellow). DLAV, dorsal longitudinal anastomotic vessel; ISV, intersegmental vessel; DA, dorsal aorta;
576 CVP, caudal vein plexus; n, notochord. (C) At 2 dpf, *nkx3.1*$^{NTR\text{-}mCherry}$-positive cells (red) were
577 observed throughout the trunk showing close association with the vasculature labeled by *kdrl:EGFP*
578 (green) (top panels). Zoomed-in views (bottom panels) show different mCherry^{+} fibroblast subtypes
579 (arrows) in four boxed regions of the trunk (i-iv). mCherry expression in muscles (asterisks) and skin
580 cells along the fin fold (arrowheads) is shown. *n*=13. (D) Most *nkx3.1*$^{NTR\text{-}mCherry}$-positive sclerotome-
581 derived cells (red) co-expressed *col1a2:GFP* (green) at 2 dpf. The upper panel shows the dorsal
582 region with dorsal fin mesenchymal cells (white arrows), DLAV fibroblasts (long cyan arrows), ISV-
583 associated perivascular fibroblasts (cyan arrows), tenocytes (magenta arrows), and interstitial
584 fibroblasts (yellow arrows). The middle panel shows DA fibroblasts (cyan arrows) associated with the
585 dorsal aorta. The bottom panel shows stromal reticular cells (cyan arrows) and ventral fin
586 mesenchymal cells (white arrows). *n*=12. Scale bars: 50 µm.

587

588 **Fig 2. Characterization of sclerotome-derived fibroblasts.** (A) The mosaic *col1a2*^{Kaede} line (green)
589 was crossed with *kdrl:mCherry* (red) to visualize the morphology of different fibroblasts at a high
590 resolution at 2 dpf: blood vessel associated fibroblasts (cyan arrows), fin mesenchymal cells (white
591 arrows), tenocytes (magenta arrow), and interstitial fibroblasts (yellow arrow). Cell processes are
592 indicated by arrowheads. The associated vascular bed and fin fold are indicated for blood vessel
593 associated fibroblasts and fin mesenchymal cells, respectively. *n*=20. (B) *nkx3.1*$^{NTR\text{-}mCherry}$*; kdrl:EGFP*
594 embryos at 53 hpf were co-stained with RFP antibody (red), GFP antibody (yellow), and probes for
595 fibroblast markers *tgfbi* or *col5a1* (cyan). mCherry^{+} blood vessel associated fibroblasts (cyan arrows),
596 tenocytes (magenta arrows), and interstitial fibroblasts (yellow arrows) co-expressed *tgfbi* and *col5a1*.
597 *n*=12 per staining. (C) *nkx3.1*$^{NTR\text{-}mCherry}$ embryos at 53 hpf were co-stained with RFP antibody (red)
598 and probes for tenocyte markers *scxa, cilp,* or *tnmd* (cyan). mCherry^{+} tenocytes (magenta arrows)
599 along MTJ co-expressed tenocyte markers. *n*=12 per staining. Scale bars: (A) 20 µm; (B, C) 50 µm.

600

601 **Fig 3. The sclerotome contributes to fin mesenchymal cells.** (A) Schematic of the zebrafish fin
602 fold. Both dorsal and ventral fin folds are populated by two adjacent cell layers: the distal
603 *hmcn2*$^{+}$*fras1*$^{+}$ apical epidermal cells and proximal *hmcn2*$^{+}$*fbln1*$^{+}$ fin mesenchymal cells. (B) Double
604 fluorescent in situ staining of *fbln1* (red) with either *fras1* or *hmcn2* (green) at 48 hpf. *fras1* labeled
605 apical epidermal cells (orange brackets), *fbln1* marked fin mesenchymal cells (white brackets), while
606 *hmcn2* was expressed in both layers. *n*=15 per staining. (C) *nkx3.1*$^{NTR\text{-}mCherry}$ embryos were costained
607 with *fbln1* or *fras1* probes (green) and anti-RFP antibody (red) at 52 hpf. Apical epidermal cells and fin
608 mesenchymal cells are indicated by arrowheads and arrows, respectively. *n*=10 per staining. (D)
609 *nkx3.1*$^{Cre\text{-}ERT2}$*; ubi:Switch* embryos treated with 4OHT at 1-2 dpf and imaged at 4 dpf. Switched
610 mCherry^{+} fin mesenchymal cells were present in the dorsal and ventral regions of the major lobe
611 (arrows) but absent in the minor lobe or caudal fin (arrowheads). *n*=10. (E) *pax7b*^{EGFP} embryos at 50
612 hpf showed extensive EGFP expression in the dermomyotome (arrow), while most fin mesenchymal
613 cells (arrowheads) in both the major and minor lobes of the fin fold were EGFP^{-}. *n*=10. (F)
614 Quantification of lineage contribution of fin mesenchymal cells. The percentage of fin mesenchymal
615 cells labeled by each lineage reporter at 2 dpf was plotted as mean±SEM. *n*=22 (*pax7b*^{EGFP}) and 13
616 (*nkx3.1*$^{NTR\text{-}mCherry}$). Statistics: Mann-Whitney *U* test; p<0.0001 (****). Scale bars: (B, D, E) 50 µm; (C)
617 20 µm.
618
619 **Fig 4. The sclerotome contributes to the axial skeleton.** (A) *nkx3.1*$^{Cre\text{-}ERT2}$*; ubi:Switch* embryos
620 were treated with 4OHT at 1-2 dpf to switch on mCherry expression (red) in sclerotome-derived cells.
621 Switched embryos were stained with calcein (cyan) at 17 dpf to visualize calcified structures, including
622 the centra (white arrowheads), neural arches (yellow arrowheads), and hemal arches (magenta
623 arrowheads). Magnified views of the neural (i) and hemal (ii) arches as well as a cross-sectional view
624 of the centrum (dotted line, iii) are shown. Switched mCherry^{+} cells associated with different skeletal
625 structures are denoted by arrows with the corresponding colors. Enrichment of mCherry^{+} cells in the
626 regions between the vertebral bodies is indicated by asterisks. Since the calcein signal is very strong,
627 un-switched GFP expression is undetectable under the imaging setting. *n*=5. (B) *nkx3.1*$^{Cre\text{-}ERT2}$*;*
628 *ubi:Switch* embryos treated with 4OHT at 1-2 dpf were raised and imaged at 6 wpf (transverse
629 section) and 1-year post-fertilization (ypf) (sagittal section). mCherry^{+} cells were associated with the
630 MTJ (magenta arrowheads), centrum (white arrowheads), neural arch (long arrows), and hemal arch
631 (short arrows). The dorsal aorta (asterisks) showed strong autofluorescence in both channels.
632 Standard lengths of imaged fish are indicated. *n*=2 per stage. (C) *nkx3.1*$^{NTR\text{-}mCherry}$ embryos and their
633 mCherry^{-} siblings were treated with MTZ at 1-2 dpf and stained with alizarin red and alcian blue at 3
634 wpf. mCherry^{+} fish showed normal vertebral bodies (arrowheads) with missing neural arches (long

635 arrow) and some misconnected hemal arches (short arrows). *n*=19 (mCherry$^-$) and 15 (mCherry$^+$). (D,
636 E) Quantification of standard length and skeletal defects in MTZ-treated fish (C). The percentage of
637 vertebrae with missing neural or hemal arches was plotted as mean±SEM. Statistics: Mann-Whitney
638 *U* test. Asterisk representation: p<0.01 (**), p<0.0001 (****). Scale bars: (A) 50 µm; (B, C) 200 µm.
639
640 **Fig 5. Lineage analysis of sclerotome domains.** (A) Schematic of lineage analysis. The entire
641 dorsal or ventral sclerotome domain in *nkx3.1^{Kaede}* embryos was photoconverted at 24 hpf and
642 analyzed for cell composition at 48 hpf. (B, C) Examples of cell tracing of the dorsal (B) and ventral
643 (C) sclerotome domains in *nkx3.1^{Kaede}* embryos. At 48 hpf, full view of the trunk and close-up views of
644 the boxed regions are shown. Cell projections at 24 hpf (arrowheads) and the outline of blood vessels
645 (dotted lines) are denoted. Pigment cells (asterisks) showed strong autofluorescence in the red
646 channel. (B) Dorsal sclerotome domain generated dorsal fin mesenchymal cells (white arrows), DLAV
647 fibroblasts (long cyan arrows), perivascular fibroblasts (cyan arrows), tenocytes (magenta arrows),
648 and interstitial fibroblasts (yellow arrows). *n*=20. (C) In the anterior somites above the yolk extension
649 (upper panel), the ventral sclerotome domain generated perivascular fibroblasts (cyan arrows),
650 tenocytes (magenta arrows), and interstitial fibroblasts (yellow arrows). In the posterior somites above
651 the CVP region (bottom panel), the ventral sclerotome domain generated SRCs (cyan arrowheads),
652 ventral fin mesenchymal cells (white arrows), tenocytes (magenta arrows), and interstitial fibroblasts
653 (yellow arrows). The ventral boundary of the CVP is indicated by dotted lines. *n*=20. Scale bars: 50
654 µm.
655
656 **Fig 6. Clonal analysis of the dorsal sclerotome.** (A) Schematic of clonal analysis. A single dorsal
657 sclerotome progenitor in *nkx3.1^{Kaede}* embryos was photoconverted at 24 hpf and imaged at 48 hpf to
658 determine clone composition. Dorsal sclerotome-derived cells were subdivided into two groups based
659 on their dorsal-ventral positions: the more dorsal type I cells include dorsal fin mesenchymal cells and
660 DLAV fibroblasts (above the dotted line), while the more ventral type II cells include tenocytes,
661 perivascular fibroblasts, and interstitial fibroblasts (below the dotted line). (B) Quantification of the
662 clone size. (C) Quantification of fibroblast subtypes in each clone. (D) Distribution of different
663 fibroblast subtypes from all decedents of traced cells. F, fin mesenchymal cells; T, tenocytes; V, blood
664 vessel associated fibroblasts; I, interstitial fibroblasts. (E) Quantification of the clone composition. Only
665 photoconverted cells showing polarized cell projections at 24 hpf were graphed. *n*=14 (with dorsal
666 projection) and 19 (with ventral projection) cells. (F) Examples of clonal analysis of dorsal sclerotome
667 progenitors in *nkx3.1^{Kaede}* embryos at 24 and 48 hpf. In the top panel (type I cell lineage), the
668 photoconverted cell showing dorsal projections (arrowhead) generated two dorsal fin mesenchymal

669 cells (white arrows) and one DLAV fibroblast (long cyan arrows). In the bottom panel (type II cell
670 lineage), the photoconverted cell with ventral cell projections (arrowhead) generated one DLAV
671 fibroblast (long cyan arrows), one perivascular fibroblast (cyan arrows), and one tenocyte (magenta
672 arrows). The outline of the vasculature is denoted by dotted lines. *n*=42 photoconverted cells from 40
673 embryos. Scale bars: 50 µm.
674
675 **Fig 7. Clonal analysis of the ventral sclerotome.** (A) Schematic of clonal analysis. A single ventral
676 sclerotome progenitor in *nkx3.1*^{Kaede} embryos was photoconverted at 24 hpf and imaged after 24 hours
677 to determine clone composition. Cells were classified as leading or lagging cells based on their initial
678 position at 24 hpf, where cells at the front of the migration path were defined as leading cells. (B)
679 Quantification of the clone composition. (C) Examples of cell tracing at 24 and 48 hpf. A lagging cell
680 (top panel) generated four SRCs (arrowheads) dorsal to the ventral edge of the CVP (dotted lines). A
681 leading cell (bottom panel) generated two fin mesenchymal cells (arrows). *n*=42 photoconverted cells
682 from 38 embryos. (D) Three mechanisms contribute to the diversification of fibroblast subtypes from
683 sclerotome progenitors in zebrafish. The fate of sclerotome progenitors is biased by their dorsal-
684 ventral or anterior-posterior positions (a, spatial regulation), migration direction (b), and migration
685 order (c). n, notochord. Scale bars: 50 µm.

686 **SUPPLEMENTAL FIGURES**

687

688 **Fig S1. Characterization of the sclerotome reporter.** Double fluorescent in situ staining of *nkx3.1*
689 (red) together with *gal4*, *kaede*, or *ntr-mcherry* (cyan) was performed in *nkx3.1*$^{NTR\text{-}mCherry}$, *nkx3.1*^{Kaede},
690 or *UAS:NTR-mCherry* embryos at 20 hpf. *gal4* expression in *nkx3.1*$^{NTR\text{-}mCherry}$ embryos accurately
691 recapitulated endogenous *nkx3.1* expression in both dorsal and ventral sclerotome domains (short
692 and long arrows, respectively). *kaede* expression in *nkx3.1*^{Kaede} embryos was largely consistent with
693 *nkx3.1* expression, whereas *nkx3.1*$^{NTR\text{-}mCherry}$ embryos showed ectopic *ntr-mcherry* expression in
694 somites (arrowheads). Note that *UAS:NTR-mCherry* but not *UAS:Kaede* embryos also showed low
695 Gal4-independent expression in the tail bud (asterisks). Representative images are shown with *n*
696 numbers for each staining. Both the merged and individual channels are shown. Scale bar: 50 µm.

697

698 **Fig S2. The sclerotome generates fin mesenchymal cells in the dorsal and ventral fin folds.** A
699 tiled confocal image of *nkx3.1*^{Kaede}*; kdrl:mCherry* embryo at 2 dpf showing Kaede^{+} sclerotome-derived
700 cells (cyan) throughout the trunk of the embryo. Kaede^{+} fin mesenchymal cells were present in both
701 dorsal and ventral fin folds (arrows), but absent from either the caudal fin or the minor lobe (asterisks).
702 Arrowheads indicate mCherry expression in skin cells at the edge of the fin fold. The major and minor
703 lobes of the fin fold are outlined by dashed lines. *n*=5. Scale bar: 200 µm.

704

705 **Fig S3. Time-lapse imaging of migration of ventral sclerotome progenitors.** Snapshots of a
706 *kdrl:EGFP; nkx3.1*$^{NTR\text{-}mCherry}$ embryo between 25 and 50 hpf are shown with timestamps (hh:mm). The
707 migration and division of two representative lagging cells (cyan arrows and arrowheads) and two
708 leading cells (white arrows and arrowheads) were traced throughout the movie. Daughter cells are
709 indicated by arrows or arrowheads in the same color. The lagging cell never migrated ahead of the
710 leading cell and generated 2 SRCs. The leading cell remained at the migration front ahead of the
711 lagging cell and generated 2 ventral fin mesenchymal cells. *n*=7. Scale bar: 50 µm.

712

713 **Video S1. Time-lapse imaging of migration of ventral sclerotome progenitors.** *kdrl:EGFP;*
714 *nkx3.1*$^{NTR\text{-}mCherry}$ embryos were imaged from 25 to 50 hpf with timestamps (hh:mm). The migration and
715 division of representative lagging (cyan arrows) and leading (white arrows) cells were traced
716 throughout the movie. Daughter cells are indicated by arrows in the same color. The lagging cell
717 never migrated ahead of the leading cell and generated 2 SRCs. The leading cell remained at the
718 migration front ahead of the lagging cell and generated 2 ventral fin mesenchymal cells. Snapshots of
719 this video are shown in Fig S3. *n*=7. Scale bar: 50 µm.

720 **REFERENCES**

721

722 **Asakawa, K., Suster, M. L., Mizusawa, K., Nagayoshi, S., Kotani, T., Urasaki, A., Kishimoto, Y.,**
723 **Hibi, M. and Kawakami, K.** (2008). Genetic dissection of neural circuits by Tol2 transposon-
724 mediated Gal4 gene and enhancer trapping in zebrafish. *Proc. Natl. Acad. Sci. U. S. A.* **105**,.

725 **Baggiolini, A., Varum, S., Mateos, J. M., Bettosini, D., John, N., Bonalli, M., Ziegler, U., Dimou,**
726 **L., Clevers, H., Furrer, R., et al.** (2015). Premigratory and migratory neural crest cells are
727 multipotent in vivo. *Cell Stem Cell* **16**, 314–322.

728 **Brent, A. E., Schweitzer, R. and Tabin, C. J.** (2003). A somitic compartment of tendon progenitors.
729 *Cell* **113**, 235–248.

730 **Buechler, M. B., Pradhan, R. N., Krishnamurty, A. T., Cox, C., Calviello, A. K., Wang, A. W.,**
731 **Yang, Y. A., Tam, L., Caothien, R., Roose-Girma, M., et al.** (2021). Cross-tissue organization
732 of the fibroblast lineage. *Nature* **593**,.

733 **Carney, T. J., Feitosa, N. M., Sonntag, C., Slanchev, K., Kluger, J., Kiyozumi, D., Gebauer, J. M.,**
734 **Talbot, J. C., Kimmel, C. B., Sekiguchi, K., et al.** (2010). Genetic analysis of fin development in
735 zebrafish identifies furin and Hemicentin1 as potential novel fraser syndrome disease genes.
736 *PLoS Genet.* **6**,.

737 **Chen, J. W. and Galloway, J. L.** (2014). The development of zebrafish tendon and ligament
738 progenitors. *Development* **141**, 2035–2045.

739 **Choi, J., Dong, L., Ahn, J., Dao, D., Hammerschmidt, M. and Chen, J. N.** (2007). FoxH1 negatively
740 modulates flk1 gene expression and vascular formation in zebrafish. *Dev. Biol.* **304**, 735–744.

741 **Christ, B., Huang, R. and Scaal, M.** (2004). Formation and differentiation of the avian sclerotome.
742 *Anat. Embryol. (Berl).* **208**,.

743 **Christ, B., Huang, R. and Scaal, M.** (2007). Amniote somite derivatives. *Dev. Dyn.* **236**,.

744 **Curado, S., Stainier, D. Y. and Anderson, R. M.** (2008). Nitroreductase-mediated cell/tissue ablation
745 in zebrafish: a spatially and temporally controlled ablation method with applications in
746 developmental and regeneration studies. *Nat Protoc* **3**, 948–954.

747 **Davison, J. M., Akitake, C. M., Goll, M. G., Rhee, J. M., Gosse, N., Baier, H., Halpern, M. E.,**
748 **Leach, S. D. and Parsons, M. J.** (2007). Transactivation from Gal4-VP16 transgenic insertions
749 for tissue-specific cell labeling and ablation in zebrafish. *Dev Biol* **304**, 811–824.

750 **Durán, I., Marí-Beffa, M., Santamaría, J. A., Becerra, J. and Santos-Ruiz, L.** (2011). Actinotrichia
751 collagens and their role in fin formation. *Dev. Biol.* **354**, 160–172.

752 **Farrell, J. A., Wang, Y., Riesenfeld, S. J., Shekhar, K., Regev, A. and Schier, A. F.** (2018). Single-
753 cell reconstruction of developmental trajectories during zebrafish embryogenesis. *Science (80-.).*

754 **360**, eaar3131.
755 **Feitosa, N. M., Zhang, J., Carney, T. J., Metzger, M., Korzh, V., Bloch, W. and Hammerschmidt,**
756 **M.** (2012). Hemicentin 2 and Fibulin 1 are required for epidermal-dermal junction formation and
757 fin mesenchymal cell migration during zebrafish development. *Dev. Biol.* **369**, 235–248.
758 **Feng, X., Adiarte, E. G. and Devoto, S. H.** (2006). Hedgehog acts directly on the zebrafish
759 dermomyotome to promote myogenic differentiation. *Dev Biol* **300**, 736–746.
760 **Fleming, A., Keynes, R. and Tannahill, D.** (2004). A central role for the notochord in vertebral
761 patterning. *Development* **131**, 873–880.
762 **Forte, E., Ramialison, M., Nim, H. T., Mara, M., Li, J. Y., Cohn, R., Daigle, S. L., Boyd, S.,**
763 **Stanley, E. G., Elefanty, A. G., et al.** (2022). Adult mouse fibroblasts retain organ-specific
764 transcriptomic identity. *Elife* **11**,.
765 **Garriock, R. J. and Krieg, P. A.** (2007). Wnt11-R signaling regulates a calcium sensitive EMT event
766 essential for dorsal fin development of Xenopus. *Dev. Biol.* **304**, 127–140.
767 **Germanguz, I., Lev, D., Waisman, T., Kim, C.-H. and Gitelman, I.** (2007). Four *twist*genes in
768 zebrafish, four expression patterns. *Dev. Dyn.* **236**, 2615–2626.
769 **Grotmol, S., Kryvi, H., Nordvik, K. and Totland, G. K.** (2003). Notochord segmentation may lay
770 down the pathway for the development of the vertebral bodies in the Atlantic salmon. *Anat.*
771 *Embryol. (Berl).* **207**,.
772 **Hammond, C. L., Hinits, Y., Osborn, D. P., Minchin, J. E., Tettamanti, G. and Hughes, S. M.**
773 (2007). Signals and myogenic regulatory factors restrict pax3 and pax7 expression to
774 dermomyotome-like tissue in zebrafish. *Dev Biol* **302**, 504–521.
775 **Inohaya, K., Takano, Y. and Kudo, A.** (2007). The teleost intervertebral region acts as a growth
776 center of the centrum: In vivo visualization of osteoblasts and their progenitors in transgenic fish.
777 *Dev. Dyn.* **236**, 3031–3046.
778 **Kalluri, R.** (2016). The biology and function of fibroblasts in cancer. *Nat. Rev. Cancer* **16**, 582–598.
779 **Kendall, R. T. and Feghali-Bostwick, C. A.** (2014). Fibroblasts in fibrosis: Novel roles and
780 mediators. *Front. Pharmacol.* **5 MAY**, 123.
781 **Kuroda, J., Itabashi, T., Iwane, A. H., Aramaki, T. and Kondo, S.** (2020). The Physical Role of
782 Mesenchymal Cells Driven by the Actin Cytoskeleton Is Essential for the Orientation of Collagen
783 Fibrils in Zebrafish Fins. *Front. Cell Dev. Biol.* **8**, 580520.
784 **Lalonde, R. L. and Akimenko, M. A.** (2018). Effects of fin fold mesenchyme ablation on fin
785 development in zebrafish. *PLoS One* **13**, e0192500.
786 **Landolt, R. M., Vaughan, L., Winterhalter, K. H. and Zimmermann, D. R.** (1995). Versican is
787 selectively expressed in embryonic tissues that act as barriers to neural crest cell migration and

788 axon outgrowth. *Development* **121**, 2303–2312.
789 **Lee, R. T. H., Knapik, E. W., Thiery, J. P. and Carney, T. J.** (2013). An exclusively mesodermal
790 origin of fin mesenchyme demonstrates that zebrafish trunk neural crest does not generate
791 ectomesenchyme. *Dev.* **140**, 2923–2932.
792 **Lleras Forero, L., Narayanan, R., Huitema, L. F. A., VanBergen, M., Apschner, A., Peterson-**
793 **Maduro, J., Logister, I., Valentin, G., Morelli, L. G., Oates, A. C., et al.** (2018). Segmentation
794 of the zebrafish axial skeleton relies on notochord sheath cells and not on the segmentation
795 clock. *Elife* **7**,.
796 **Ma, R. C., Jacobs, C. T., Sharma, P., Kocha, K. M. and Huang, P.** (2018). Stereotypic generation of
797 axial tenocytes from bipartite sclerotome domains in zebrafish. *PLoS Genet.* **14**, e1007775.
798 **Mahabaleshwar, H., Asharani, P. V, Loo, T. Y., Koh, S. Y., Pitman, M. R., Kwok, S., Ma, J., Hu,**
799 **B., Lin, F., Li Lok, X., et al.** (2022). Slit-Robo signalling establishes a Sphingosine-1-phosphate
800 gradient to polarise fin mesenchyme. *EMBO Rep.* **23**, e54464.
801 **Metikala, S., Chetty, S. C. and Sumanas, S.** (2021). Single-cell transcriptome analysis of the
802 zebrafish embryonic trunk. *PLoS One* **16**,.
803 **Minchin, J. E. N. and Hughes, S. M.** (2008). Sequential actions of Pax3 and Pax7 drive xanthophore
804 development in zebrafish neural crest. *Dev. Biol.* **317**,.
805 **Mise, T., Iijima, M., Inohaya, K., Kudo, A. and Wada, H.** (2008). Function of Pax1 and Pax9 in the
806 sclerotome of medaka fish. *Genesis* **46**,.
807 **Morin-Kensicki, E. M. and Eisen, J. S.** (1997). Sclerotome development and peripheral nervous
808 system segmentation in embryonic zebrafish. *Development* **124**, 159–167.
809 **Morin-Kensicki, E. M., Melancon, E. and Eisen, J. S.** (2002). Segmental relationship between
810 somites and vertebral column in zebrafish. *Development* **129**, 3851–3860.
811 **Mosimann, C., Kaufman, C. K., Li, P., Pugach, E. K., Tamplin, O. J. and Zon, L. I.** (2011).
812 Ubiquitous transgene expression and Cre-based recombination driven by the ubiquitin promoter
813 in zebrafish. *Development* **138**, 169–177.
814 **Muhl, L., Genové, G., Leptidis, S., Liu, J., He, L., Mocci, G., Sun, Y., Gustafsson, S.,**
815 **Buyandelger, B., Chivukula, I. V, et al.** (2020). Single-cell analysis uncovers fibroblast
816 heterogeneity and criteria for fibroblast and mural cell identification and discrimination. *Nat.*
817 *Commun.* **11**, 3953.
818 **Murayama, E., Sarris, M., Redd, M., Le Guyader, D., Vivier, C., Horsley, W., Trede, N. and**
819 **Herbomel, P.** (2015). NACA deficiency reveals the crucial role of somite-derived stromal cells in
820 haematopoietic niche formation. *Nat. Commun.* **6**, 8375.
821 **Nguyen, P. D., Hollway, G. E., Sonntag, C., Miles, L. B., Hall, T. E., Berger, S., Fernandez, K. J.,**

822 **Gurevich, D. B., Cole, N. J., Alaei, S., et al.** (2014). Haematopoietic stem cell induction by
823 somite-derived endothelial cells controlled by meox1. *Nature* **512**,.
824 **Parichy, D. M., Elizondo, M. R., Mills, M. G., Gordon, T. N. and Engeszer, R. E.** (2009). Normal
825 table of postembryonic zebrafish development: Staging by externally visible anatomy of the living
826 fish. *Dev. Dyn.* **238**, 2975–3015.
827 **Pipalia, T. G., Koth, J., Roy, S. D., Hammond, C. L., Kawakami, K. and Hughes, S. M.** (2016).
828 Cellular dynamics of regeneration reveals role of two distinct Pax7 stem cell populations in larval
829 zebrafish muscle repair. *Dis Model Mech* **9**, 671–684.
830 **Plikus, M. V., Wang, X., Sinha, S., Forte, E., Thompson, S. M., Herzog, E. L., Driskell, R. R.,**
831 **Rosenthal, N., Biernaskie, J. and Horsley, V.** (2021). Fibroblasts: Origins, definitions, and
832 functions in health and disease. *Cell* **184**,.
833 **Pogoda, H. M., Riedl-Quinkertz, I., Löhr, H., Waxman, J. S., Dale, R. M., Topczewski, J., Schulte-**
834 **Merker, S. and Hammerschmidt, M.** (2018). Direct activation of chordoblasts by retinoic acid is
835 required for segmented centra mineralization during zebrafish spine development. *Dev.* **145**,.
836 **Pouget, C., Pottin, K. and Jaffredo, T.** (2008). Sclerotomal origin of vascular smooth muscle cells
837 and pericytes in the embryo. *Dev. Biol.* **315**, 437–47.
838 **Proulx, K., Lu, A. and Sumanas, S.** (2010). Cranial vasculature in zebrafish forms by angioblast
839 cluster-derived angiogenesis. *Dev. Biol.* **348**,.
840 **Rajan, A. M., Ma, R. C., Kocha, K. M., Zhang, D. J. and Huang, P.** (2020). Dual function of
841 perivascular fibroblasts in vascular stabilization in zebrafish. *PLoS Genet.* **16**, e1008800.
842 **Ralliere, C., Fretaud, M., Thermes, V. and Rescan, P. Y.** (2015). CILP1 is dynamically expressed in
843 the developing musculoskeletal system of the trout. *Int J Dev Biol* **59**, 505–509.
844 **Rocha, M., Beiriger, A., Kushkowski, E. E., Miyashita, T., Singh, N., Venkataraman, V. and**
845 **Prince, V. E.** (2020). From head to tail: regionalization of the neural crest. *Development* **147**,.
846 **Sahai-Hernandez, P., Pouget, C., Svoboda, O. and Traver, D.** (2020). Dermomyotome-derived
847 endothelial cells migrate to the dorsal aorta to support hematopoietic stem cell emergence.
848 *bioRxiv* 2020.05.14.096305.
849 **Schindelin, J., Arganda-Carreras, I., Frise, E., Kaynig, V., Longair, M., Pietzsch, T., Preibisch,**
850 **S., Rueden, C., Saalfeld, S., Schmid, B., et al.** (2012). Fiji: an open-source platform for
851 biological-image analysis. *Nat. Methods* **9**, 676–82.
852 **Schneider, A., Brand, T., Zweigerdt, R. and Arnold, H.** (2000). Targeted disruption of the Nkx3.1
853 gene in mice results in morphogenetic defects of minor salivary glands: parallels to glandular
854 duct morphogenesis in prostate. *Mech. Dev.* **95**, 163–174.
855 **Schweitzer, R., Chyung, J. H., Murtaugh, L. C., Brent, A. E., Rosen, V., Olson, E. N., Lassar, A.**

856 **and Tabin, C. J.** (2001). Analysis of the tendon cell fate using Scleraxis, a specific marker for
857 tendons and ligaments. *Development* **128**, 3855–3866.
858 **Sharma, P., Ruel, T. D., Kocha, K. M., Liao, S. and Huang, P.** (2019). Single cell dynamics of
859 embryonic muscle progenitor cells in zebrafish. *Development* **146**, dev178400.
860 **Smith, M. M. and Hall, B. K.** (1990). Development and evolutionary origins of vertebrate skeletogenic
861 and odontogenic tissues. *Biol. Rev. Camb. Philos. Soc.* **65**, 277–373.
862 **Smith, M., Hickman, A., Amanze, D., Lumsden, A. and Thorogood, P.** (1994). Trunk neural crest
863 origin of caudal fin mesenchyme in the zebrafish Brachydanio rerio. *Proc. R. Soc. B Biol. Sci.*
864 **256**, 137–145.
865 **Sobkow, L., Epperlein, H. H., Herklotz, S., Straube, W. L. and Tanaka, E. M.** (2006). A germline
866 GFP transgenic axolotl and its use to track cell fate: Dual origin of the fin mesenchyme during
867 development and the fate of blood cells during regeneration. *Dev. Biol.* **290**, 386–397.
868 **Subramanian, A. and Schilling, T. F.** (2014). Thrombospondin-4 controls matrix assembly during
869 development and repair of myotendinous junctions. *Elife* **3**,.
870 **Subramanian, A., Kanzaki, L. F., Galloway, J. L. and Schilling, T. F.** (2018). Mechanical force
871 regulates tendon extracellular matrix organization and tenocyte morphogenesis through TGFbeta
872 signaling. *Elife* **7**,.
873 **Tabib, T., Morse, C., Wang, T., Chen, W. and Lafyatis, R.** (2018). SFRP2/DPP4 and FMO1/LSP1
874 Define Major Fibroblast Populations in Human Skin. *J. Invest. Dermatol.* **138**, 802–810.
875 **Tallquist, M. D.** (2020). Developmental pathways of cardiac fibroblasts. *Cold Spring Harb. Perspect.*
876 *Biol.* **12**,.
877 **Taniguchi, Y., Kurth, T., Medeiros, D. M., Tazaki, A., Ramm, R. and Epperlein, H. H.** (2015).
878 Mesodermal origin of median fin mesenchyme and tail muscle in amphibian larvae. *Sci. Rep.* **5**,
879 11428.
880 **Thulabandu, V., Chen, D. and Atit, R. P.** (2018). Dermal fibroblast in cutaneous development and
881 healing. *Wiley Interdiscip. Rev. Dev. Biol.* **7**,.
882 **Topczewska, J. M., Topczewski, J., Solnica-Krezel, L. and Hogan, B. L. M.** (2001). Sequence and
883 expression of zebrafish foxc1a and foxc1b, encoding conserved forkhead/winged helix
884 transcription factors. *Mech. Dev.* **100**,.
885 **Tucker, A. S. and Slack, J. M. W.** (2004). Independent induction and formation of the dorsal and
886 ventral fins in Xenopus laevis. *Dev. Dyn.* **230**, 461–467.
887 **Walker, M. B. and Kimmel, C. B.** (2007). A two-color acid-free cartilage and bone stain for zebrafish
888 larvae. *Biotech. Histochem.* **82**,.
889 **Wang, S., Kryvi, H., Grotmol, S., Wargelius, A., Krossøy, C., Epple, M., Neues, F., Furmanek, T.**

890 **and Totland, G. K.** (2013). Mineralization of the vertebral bodies in Atlantic salmon (Salmo salar
891 L.) is initiated segmentally in the form of hydroxyapatite crystal accretions in the notochord
892 sheath. *J. Anat.* **223**,.
893 **Wattrus, S. J. and Zon, L. I.** (2018). Stem cell safe harbor: The hematopoietic stem cell niche in
894 zebrafish. *Blood Adv.* **2**, 3063–3069.
895 **Wiegreffe, C., Christ, B., Huang, R. and Scaal, M.** (2007). Sclerotomal origin of smooth muscle cells
896 in the wall of the avian dorsal aorta. *Dev. Dyn.* **236**, 2578–2585.
897 **Wopat, S., Bagwell, J., Sumigray, K. D., Dickson, A. L., Huitema, L. F. A., Poss, K. D., Schulte-**
898 **Merker, S. and Bagnat, M.** (2018). Spine Patterning Is Guided by Segmentation of the
899 Notochord Sheath. *Cell Rep.* **22**, 2026–2038.
900 **Xie, T., Wang, Y., Deng, N., Huang, G., Taghavifar, F., Geng, Y., Liu, N., Kulur, V., Yao, C., Chen,**
901 **P., et al.** (2018). Single-Cell Deconvolution of Fibroblast Heterogeneity in Mouse Pulmonary
902 Fibrosis. *Cell Rep.* **22**, 3625–3640.
903 **Yasutake, J., Inohaya, K. and Kudo, A.** (2004). Twist functions in vertebral column formation in
904 medaka, Oryzias latipes. *Mech. Dev.* **121**, 883–894.
905 **Yeo, G. H., Cheah, F. S. H., Winkler, C., Jabs, E. W., Venkatesh, B. and Chong, S. S.** (2009).
906 Phylogenetic and evolutionary relationships and developmental expression patterns of the
907 zebrafish twist gene family. *Dev. Genes Evol.* **219**,.
908

Figure 1

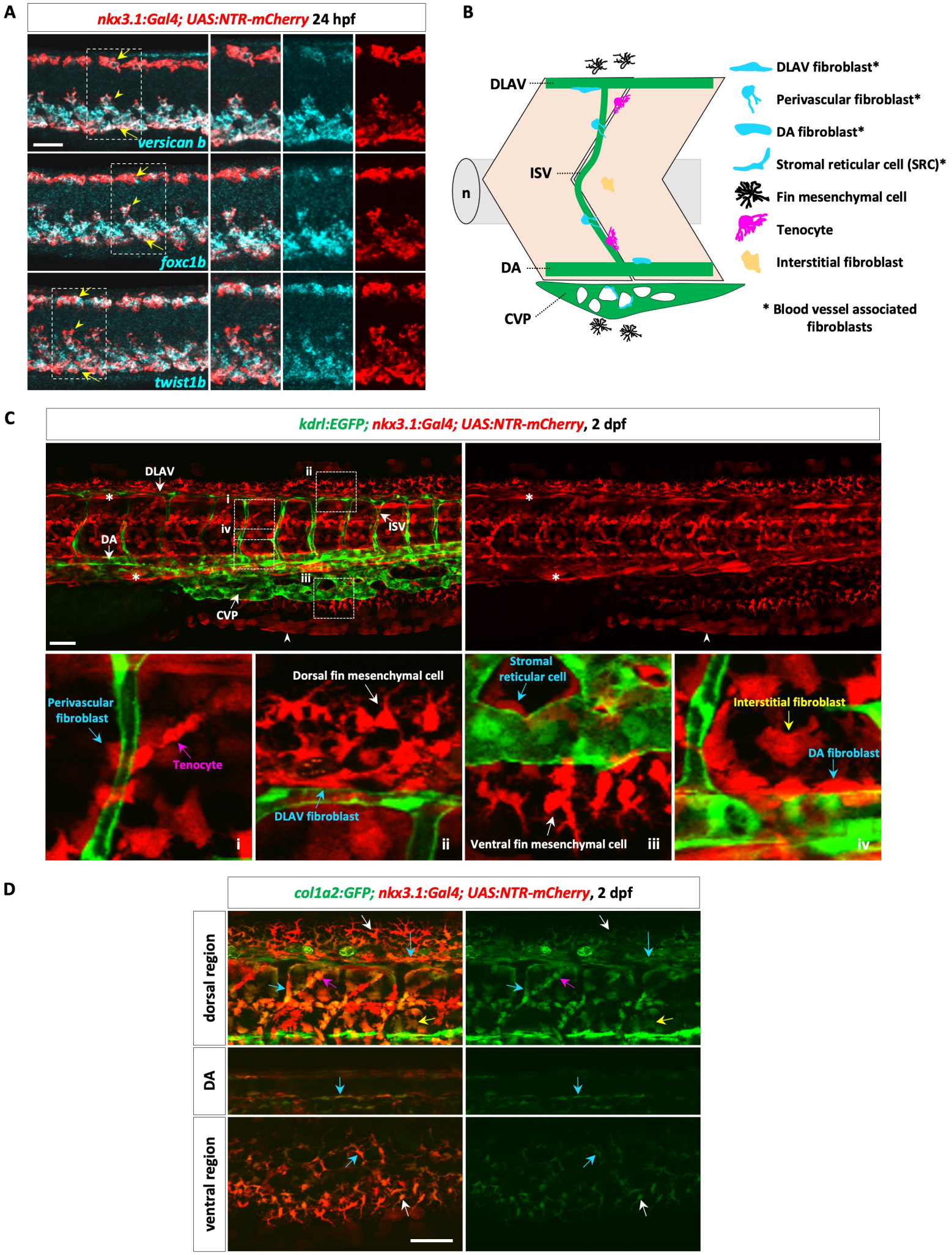
A
nkx3.1:Gal4; UAS:NTR-mCherry 24 hpf
versican b
foxc1b
twist1b
B
DLAV
ISV
n
DA
CVP
DLAV fibroblast*
Perivascular fibroblast*
DA fibroblast*
Stromal reticular cell (SRC)*
Fin mesenchymal cell
Tenocyte
Interstitial fibroblast
* Blood vessel associated fibroblasts
C
kdrl:EGFP; nkx3.1:Gal4; UAS:NTR-mCherry, 2 dpf
DLAV
DA
CVP
ISV
i
ii
iii
iv
Perivascular fibroblast
Tenocyte
Dorsal fin mesenchymal cell
DLAV fibroblast
Stromal reticular cell
Ventral fin mesenchymal cell
Interstitial fibroblast
DA fibroblast
D
col1a2:GFP; nkx3.1:Gal4; UAS:NTR-mCherry, 2 dpf
dorsal region
DA
ventral region

Figure 2

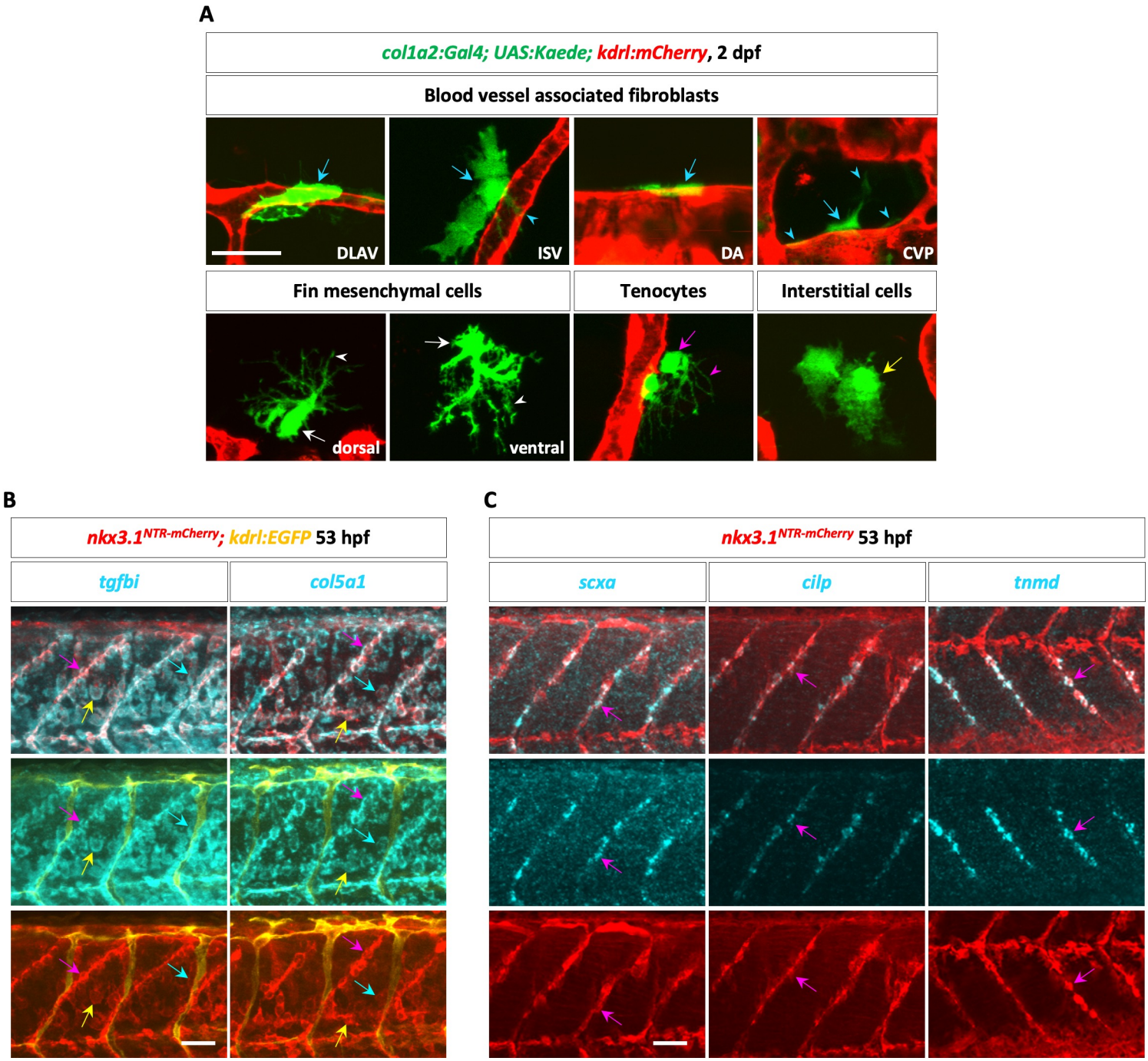
A
col1a2:Gal4; UAS:Kaede; kdrl:mCherry, 2 dpf
Blood vessel associated fibroblasts
DLAV
ISV
DA
CVP
Fin mesenchymal cells
Tenocytes
Interstitial cells
dorsal
ventral
B
nkx3.1NTR-mCherry; kdrl:EGFP 53 hpf
tgfbi
col5a1
C
nkx3.1NTR-mCherry 53 hpf
scxa
cilp
tnmd

Figure 3

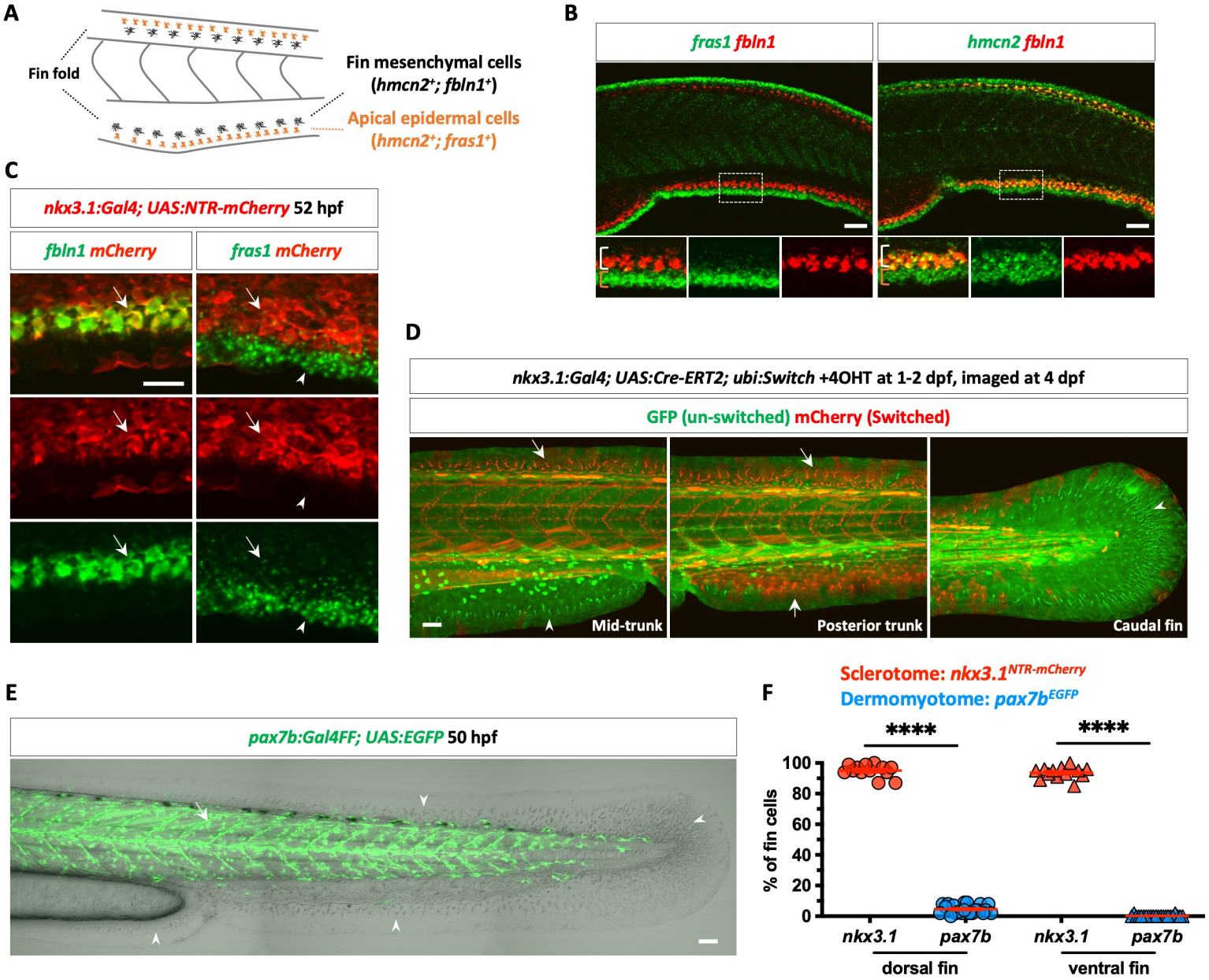
A
Fin fold
Fin mesenchymal cells
(hmcn2+; fbln1+)
Apical epidermal cells
(hmcn2+; fras1+)
B
fras1 fbln1
hmcn2 fbln1
C
nkx3.1:Gal4; UAS:NTR-mCherry 52 hpf
fbln1 mCherry
fras1 mCherry
D
nkx3.1:Gal4; UAS:Cre-ERT2; ubi:Switch +4OHT at 1-2 dpf, imaged at 4 dpf
GFP (un-switched) mCherry (Switched)
Mid-trunk
Posterior trunk
Caudal fin
E
pax7b:Gal4FF; UAS:EGFP 50 hpf
F
Sclerotome: nkx3.1NTR-mCherry
Dermomyotome: pax7bEGFP
****
****
% of fin cells
100
80
60
40
20
0
nkx3.1
pax7b
nkx3.1
pax7b
dorsal fin
ventral fin

Figure 4

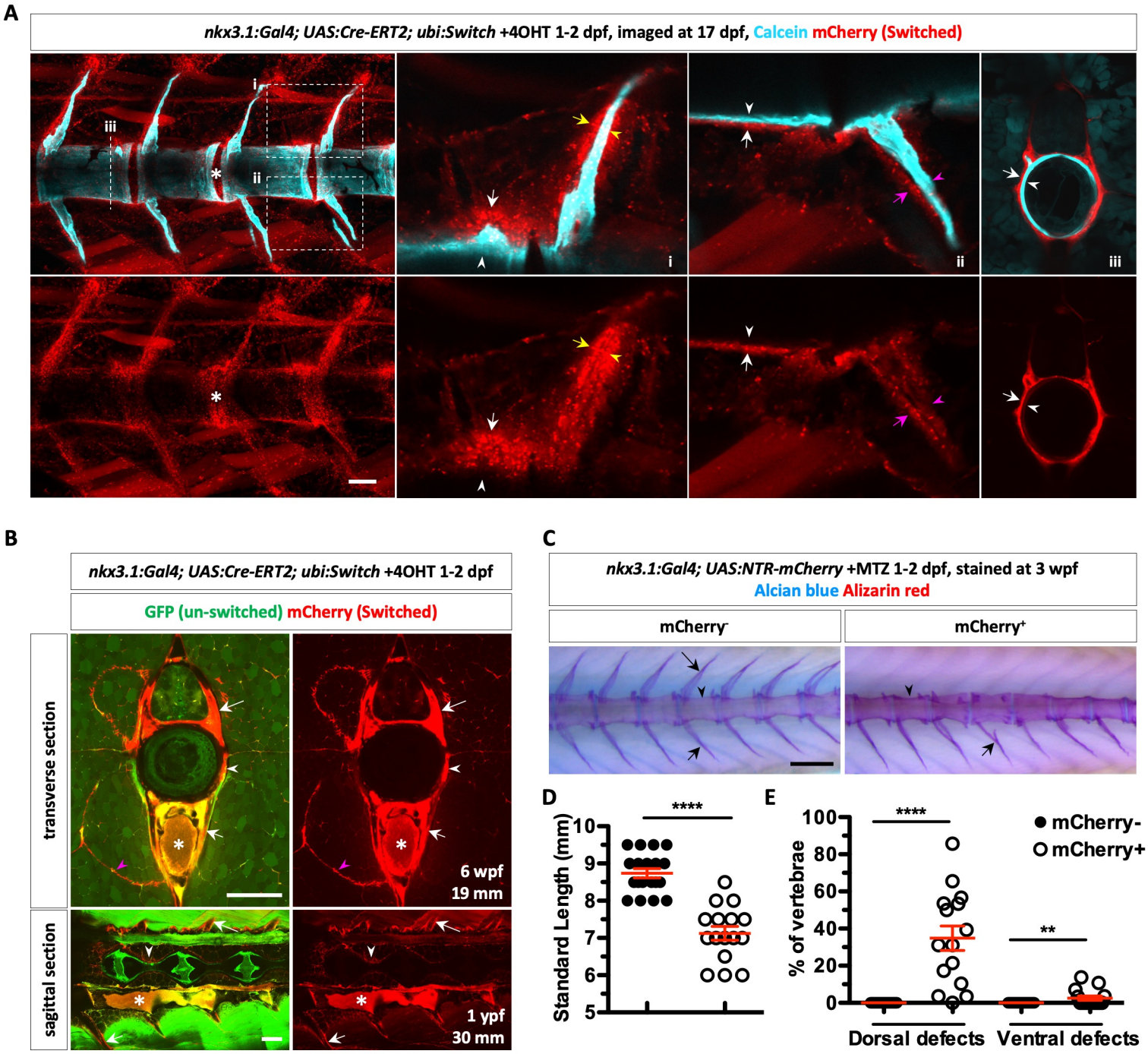
A
nkx3.1:Gal4; UAS:Cre-ERT2; ubi:Switch +4OHT 1-2 dpf, imaged at 17 dpf, Calcein mCherry (Switched)
i
ii
iii
B
nkx3.1:Gal4; UAS:Cre-ERT2; ubi:Switch +4OHT 1-2 dpf
GFP (un-switched) mCherry (Switched)
transverse section
sagittal section
6 wpf
19 mm
1 ypf
30 mm
C
nkx3.1:Gal4; UAS:NTR-mCherry +MTZ 1-2 dpf, stained at 3 wpf
Alcian blue Alizarin red
mCherry-
mCherry+
D
Standard Length (mm)
****
E
% of vertebrae
****
**
mCherry-
mCherry+
Dorsal defects
Ventral defects

Figure 5

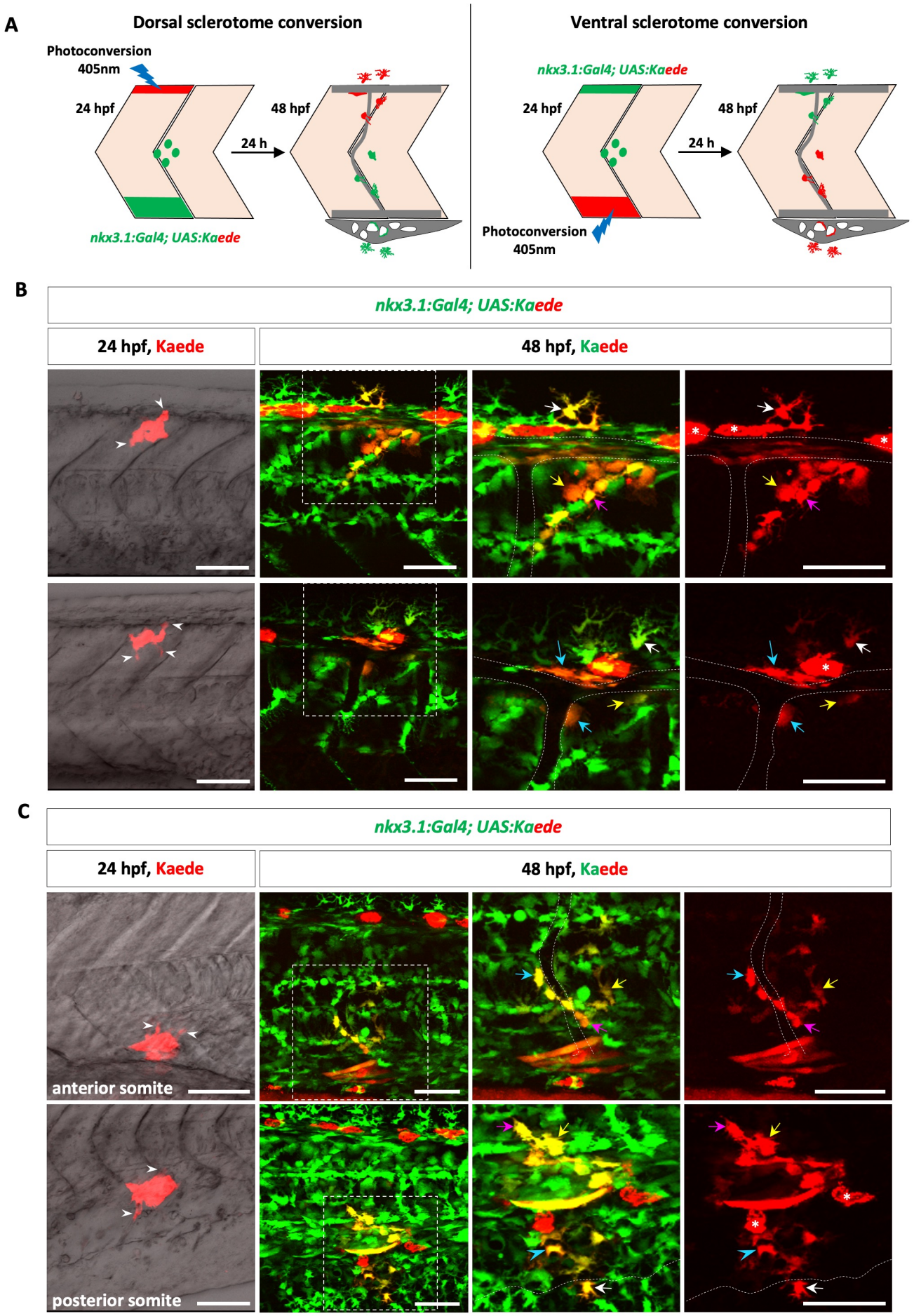
A
Dorsal sclerotome conversion
Photoconversion
405nm
24 hpf
48 hpf
24 h
nkx3.1:Gal4; UAS:Kaede
Ventral sclerotome conversion
nkx3.1:Gal4; UAS:Kaede
24 hpf
48 hpf
24 h
Photoconversion
405nm
B
nkx3.1:Gal4; UAS:Kaede
24 hpf, Kaede
48 hpf, Kaede
C
nkx3.1:Gal4; UAS:Kaede
24 hpf, Kaede
48 hpf, Kaede
anterior somite
posterior somite

Figure 6

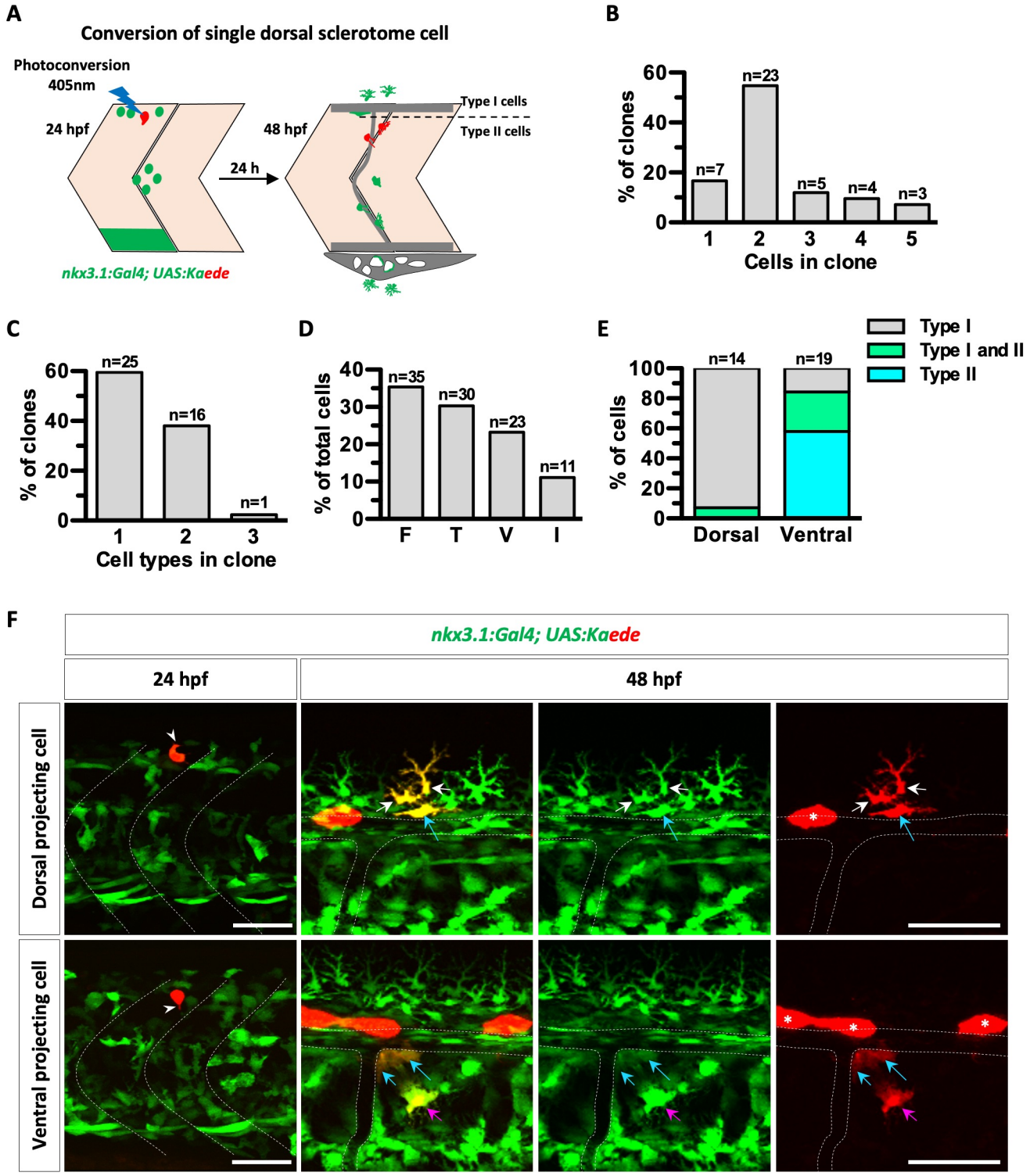
A
Conversion of single dorsal sclerotome cell
Photoconversion
405nm
24 hpf
24 h
48 hpf
Type I cells
Type II cells
nkx3.1:Gal4; UAS:Kaede
B
% of clones
Cells in clone
n=7
n=23
n=5
n=4
n=3
C
% of clones
Cell types in clone
n=25
n=16
n=1
D
% of total cells
F
T
V
I
n=35
n=30
n=23
n=11
E
% of cells
Dorsal
Ventral
n=14
n=19
Type I
Type I and II
Type II
F
nkx3.1:Gal4; UAS:Kaede
24 hpf
48 hpf
Dorsal projecting cell
Ventral projecting cell

Figure 7

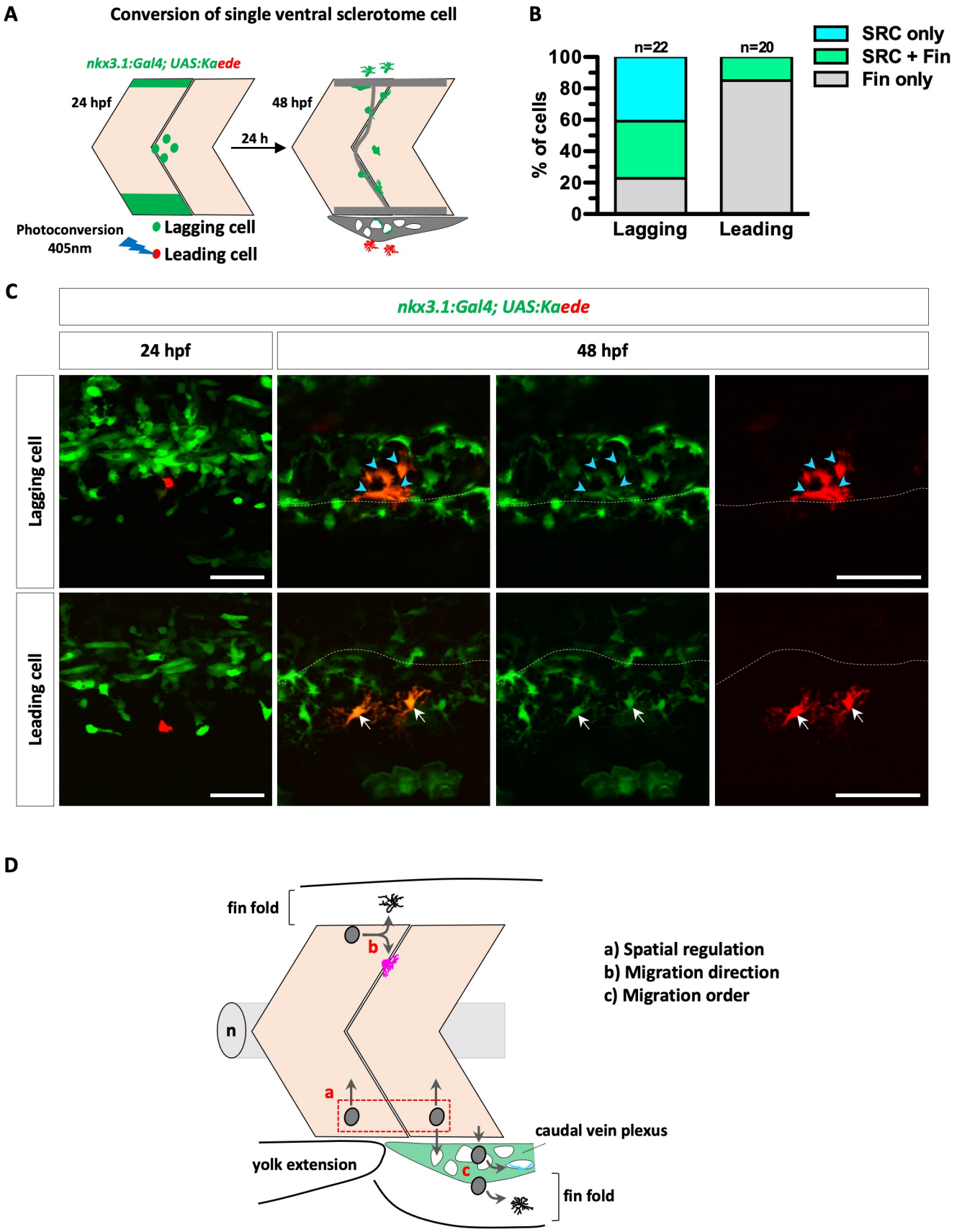
A
Conversion of single ventral sclerotome cell
nkx3.1:Gal4; UAS:Kaede
24 hpf
48 hpf
24 h
Photoconversion
405nm
Lagging cell
Leading cell
B
SRC only
SRC + Fin
Fin only
n=22
n=20
% of cells
100
80
60
40
20
0
Lagging
Leading
C
nkx3.1:Gal4; UAS:Kaede
24 hpf
48 hpf
Lagging cell
Leading cell
D
fin fold
b
n
a
caudal vein plexus
yolk extension
c
fin fold
a) Spatial regulation
b) Migration direction
c) Migration order

Figure S1

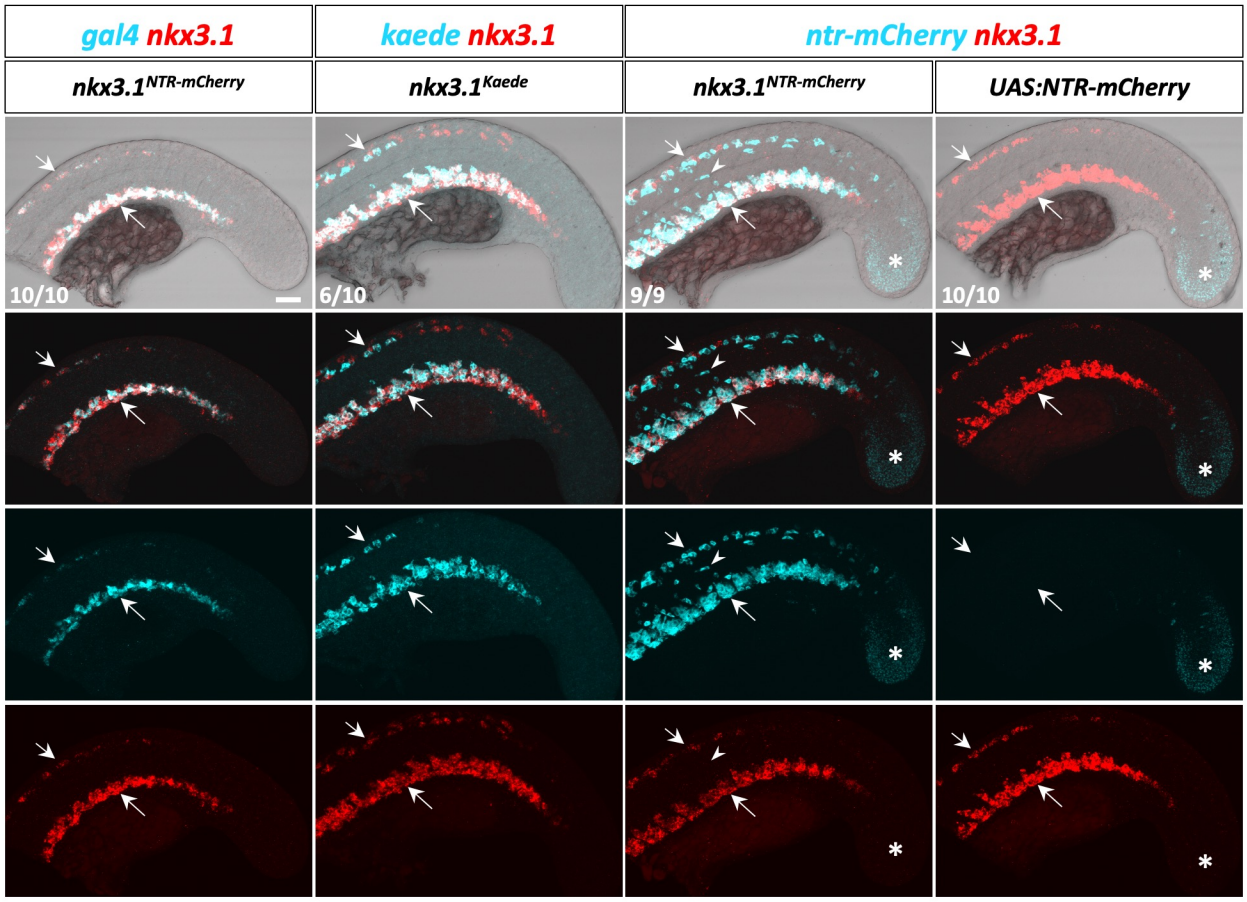
gal4 nkx3.1
kaede nkx3.1
ntr-mCherry nkx3.1
nkx3.1NTR-mCherry
nkx3.1Kaede
nkx3.1NTR-mCherry
UAS:NTR-mCherry
10/10
6/10
9/9
10/10

Figure S2

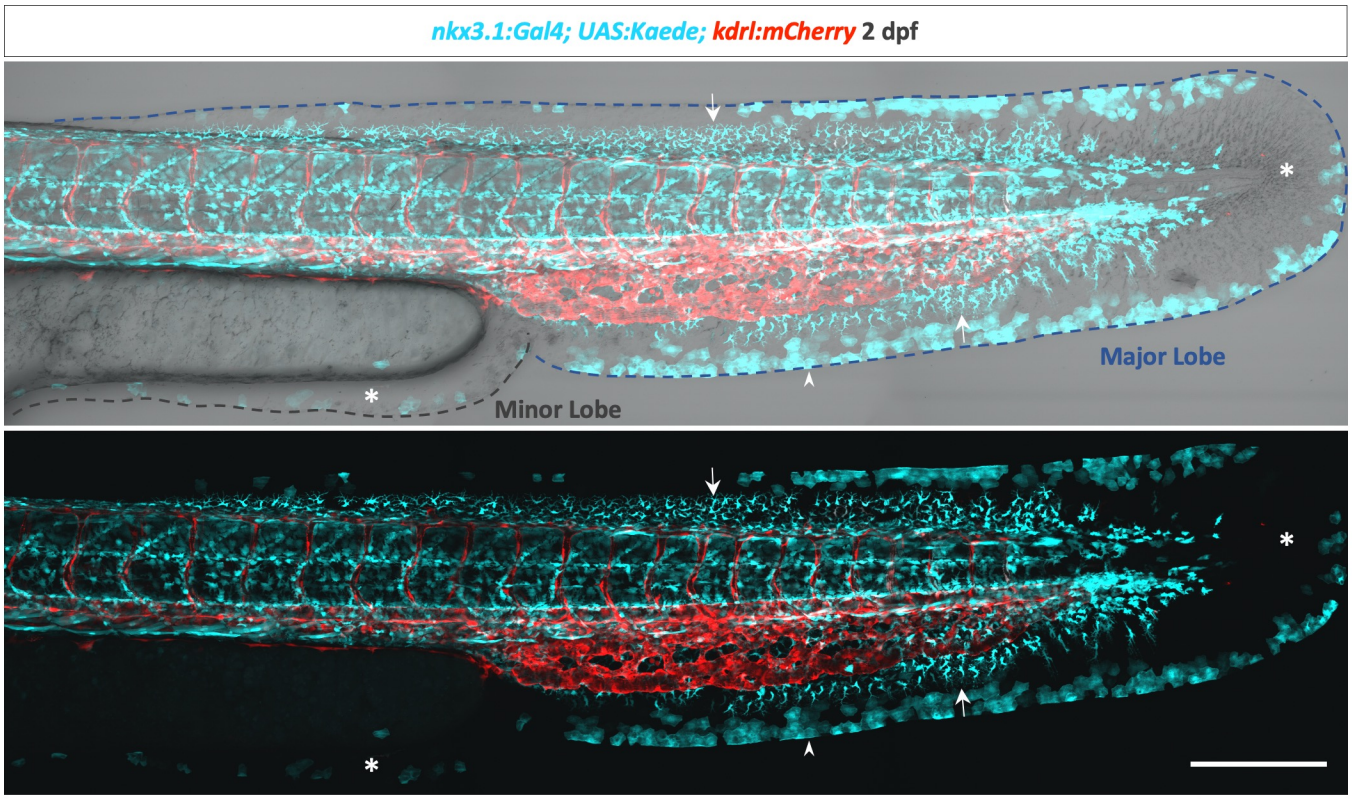
nkx3.1:Gal4; UAS:Kaede; kdrl:mCherry 2 dpf
Major Lobe
Minor Lobe

Figure S3

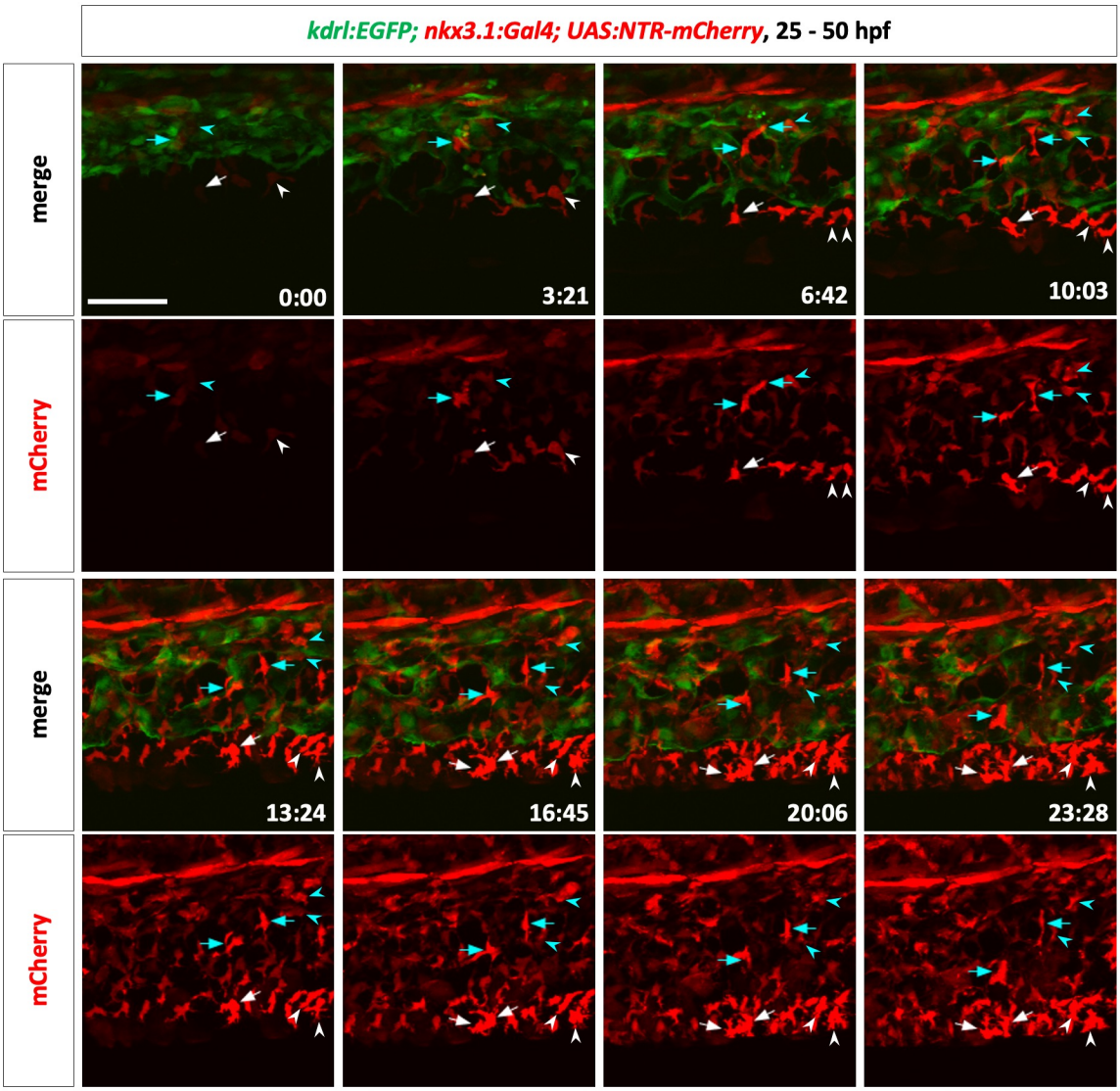
kdrl:EGFP; nkx3.1:Gal4; UAS:NTR-mCherry, 25 - 50 hpf
merge
mCherry
merge
mCherry
0:00
3:21
6:42
10:03
13:24
16:45
20:06
23:28